MDPI

Review

A Review on Strain Study of Cuprate Superconductors

Jian Zhang [1,2,*,†] ![ORCID], **Haiyan Wu** [1,2,†], **Guangzhen Zhao** [2], **Lu Han** [2] **and Jun Zhang** [3,*]

1 Institute of Environmental Research at Greater Bay Area, Key Laboratory for Water Quality and Conservation of the Pearl River Delta, Ministry of Education, Guangzhou University, Guangzhou 510006, China

2 Key Laboratory of Spin Electron and Nanomaterials of Anhui Higher Education Institutes, Suzhou University, Suzhou 234000, China

3 School of Pharmacy, Dali University, Dali 671000, China

* Correspondence: zhangjianno01@163.com (J.Z.); super_junzai008@163.com (J.Z.)

† These authors contributed equally to this work.

Abstract: Cuprate superconductors have attracted extensive attention due to their broad promising application prospects. Among the factors affecting superconductivity, the effect of strain cannot be ignored, which can significantly enhance or degrade superconductivity. In this review, we discuss and summarize the methods of applying strain to cuprate superconductors, strain measurement techniques, and the influence of strain on superconductivity. Among them, we pay special attention to the study of strain in high–temperature superconducting (HTS) films and coating. We expect this review can guide further research in the field of cuprate superconductors.

Keywords: cuprate superconductors; lattice mismatch; strain; heterointerface

1. Introduction

Superconductors have two defining properties: (1) vanishing of electrical resistivity below a critical transition temperature (T_c) and (2) expulsion of magnetic flux below a critical field (H_c). The former was discovered by Kamerlingh–Onnes in 1911, and the latter by Meissner and Ochsenfeld in 1933. $YBa_2Cu_3O_{7-\delta}$ (YBCO) was the first discovered superconductor that has T_c above the liquid N_2 temperature (77 K) [1]. YBCO's discovery fueled a great deal of research activity in superconductivity. Initially, most research focused on developing superconductors with a higher T_c and critical current density (J_c). Subsequently, other superconductors such as $HgBa_2Ca_2Cu_3O_{8+\delta}$ [2] (HgBCCO), $Tl_2Ba_2Ca_2Cu_3O_{10+\delta}$ [3] (TlBCCO), and $Bi_2Sr_2Ca_2Cu_3O_{10+\delta}$ [4] (BSCCO) have also been discovered that had T_cs above 77 K. Since the common property of all these materials was the layered crystal structure that contained one or more CuO_2 planes, they were called "cuprates", which are structurally, chemically, and/or electronically inhomogeneous at the nanoscale.

It is believed that high–temperature superconductors (HTSs) are most suitable for fabricating a lot of potential applications, including motors, magnetic and flywheel energy storage systems, wind generators, magnetic resonance image (MRI), fault current limiters, filters, superconducting quantum interference devices (SQUIDs), and so on [5–7]. The field of applied, technological superconductivity is now moving beyond these preliminary demonstrators to the industrial development of commercially viable machines and devices. Strain is a key parameter for understanding many physical phenomena at the nanoscale. The mechanical and electronic properties of a material are directly related to the strain in the material, and the response of a material to an applied strain is fundamental to the engineering of mechanical or electronic properties. Superconducting performance is strongly influenced by strain, which is an unexpected phenomenon [8]. Researchers have spent a considerable amount of time investigating the strain to gain a deeper understanding of its relationship with the film's superconducting performance [9]. For $La_{1.9}Sr_{0.1}CuO_4$ superconducting films deposited on $LaSrAlO_4$ substrates, the compressive epitaxial strain caused by lattice mismatch doubled T_c [10]. Researchers have observed that anomalous

strain fields surrounding misfit dislocations can change the functional properties of oxide heterointerface structures [11,12]. A decrease in J_c with increasing axial tension or compression in self-field has also been observed in YBCO [13–15]. It has been shown in theoretical studies that modulating the heterointerface strain can either improve [16–18] or demolish the superconductivity [19]. Therefore, the widespread application of HTSs requires an in-depth understanding of the relationship between composition, functionality, and microstructure.

Our review aims to provide an overview of recent advances in strain studies related to cuprate superconductors. In the first section, we summarize the various methods currently available for applying strain to superconducting materials; the second section describes the diverse characterization techniques for measuring strain; the third section presents a comprehensive description of the influence of strain on superconducting properties. Finally, the challenges and development prospects of current theoretical studies on the impact of strain on superconductivity are discussed.

2. Strain Application Methods

For superconducting tapes or wires, the strain can be applied by stretching with a motor, as shown in Figure 1. The sample is stretched by mechanical motion to obtain the superconducting performance under strain. However, this approach cannot be applied to HTS films. HTS films are deposited on single crystal substrates that are brittle and will break in the stretched state, failing the experiment. Fortunately, owing to the lattice parameter difference between substrates and films, it is an effective way to apply lattice mismatch to introduce strain into HTS films and study the influence of strain on the superconductivity of HTS films, as shown in Figure 2. Biaxial pressures can be imposed by strain relaxation mechanisms caused by lattice mismatch between films and substrates, which either increases or reduces T_c [20]. In addition, in artificial flux pinning centers (APCs) studies of HTSs, strain is also generated between the secondary phase and HTS matrix due to lattice mismatch. This is also a very important research direction in the vortex pinning study of HTSs.
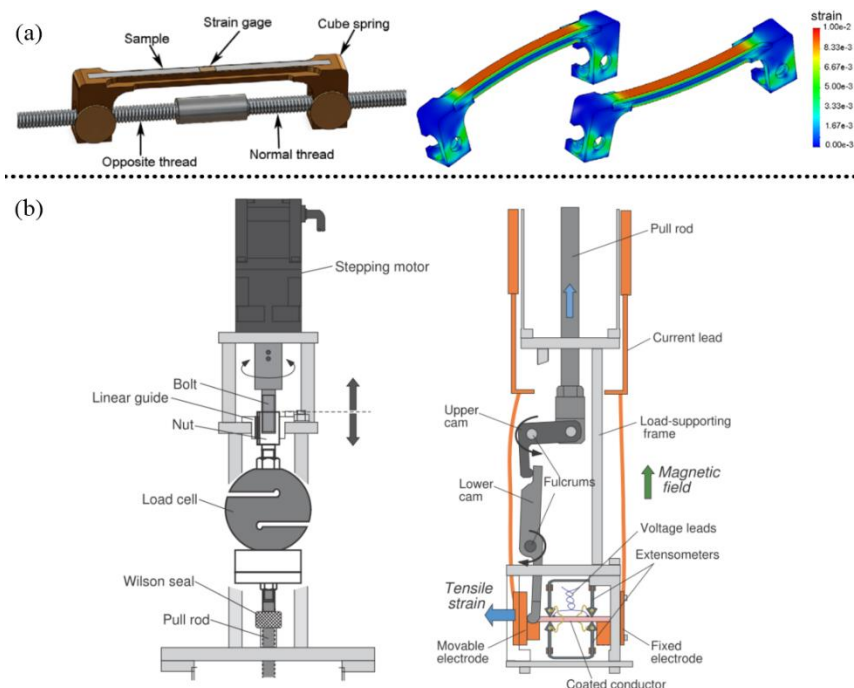

Figure 1. (**a**,**b**) Different methods of applying strain. Reprinted with permission from Refs. [14,21]. Copyright 2007, AIP Publishing; copyright 2010, IOP Publishing Ltd.
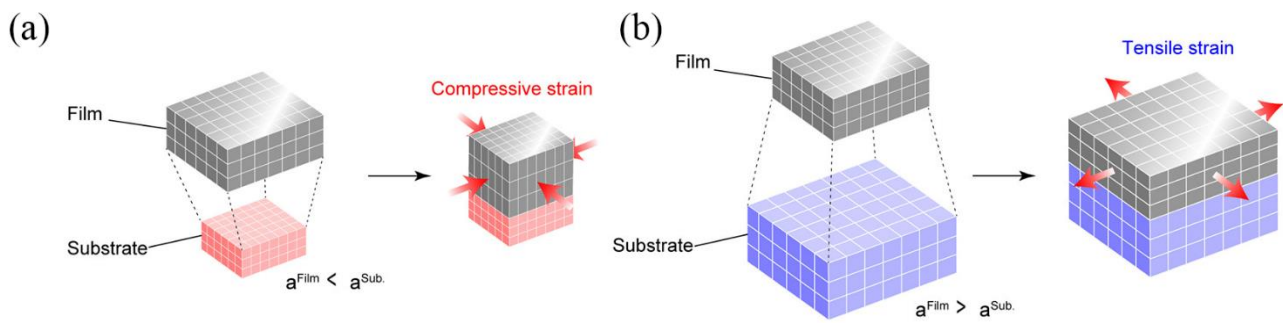
Figure 2. (**a**) $a^{\text{Film}} < a^{\text{Sub}}$; compressive strain. (**b**) $a^{\text{Film}} > a^{\text{Sub}}$; tensile strain. Adapted with permission from Ref. [22]. Copyright 2020, American Chemical Society.

3. Strain Measurement Techniques

At present, the strain measurement techniques for HTS are relatively mature, mainly including X-ray diffraction (XRD)/ Transmission electron microscope (TEM)/Raman/Neutron Diffraction/Electron backscatter diffraction (EBSD), etc. In this section, we briefly summarize the relevant applications in strain studies of superconductors.

3.1. XRD

Jingfeng Yu et al. [23] investigated YBCO films prepared on $(LaAlO_3)_{0.3}$-$(Sr_2AlTaO_6)_{0.7}$ (LSAT), $SrTiO_3$, and $LaAlO_3$ substrates, and the corresponding influence on superconductivity. Internal strain and residual stress were measured by an extended small-angle $\sin^2\psi$ method and the Williamson-Hall plot method, respectively. It was confirmed that $YBCO/LaAlO_3$ samples exhibited compressive stress, but YBCO/LSAT and $YBCO/SrTiO_3$ samples exhibited tensile stress. The results of their study demonstrated that T_c had the same variation trend as strain. They suggested that controlling adequate microscopic internal strain and macroscopic residual stress are critical to tailoring microstructures and superconductivity.

Ziliang Li et al. [24] studied the superconducting properties and microstructure of chemical solution deposited (CSD) YBCO films by XRD measurements and magnetic susceptibility. With film thickness decreasing down to 5 nm, the effect of $Y_2Ba_4Cu_8O_{16}$ intergrowth in films was revealed. Ultrathin films offer a unique opportunity to investigate the superconducting properties of highly concentrated nanoscale defects due to the elastic energy related to the misfit strain. Their results demonstrated that superconducting volume decreased strongly correlated with intergrowth volume fraction increasing. Furthermore, they proved that these intergrowths were non-superconducting nanoscale regions that suppressed Cooper pair formation, supporting their role as vortex pining in YBCO films and coated conductors.

3.2. Neutron Diffraction

Kozo Osamura et al. [25] precisely investigated the strain of YBCO coated conductors and their corresponding effect on critical current (I_c). The internal strain of the YBCO layer was characterized at 77 K by the neutron diffraction technique. The force-free strain (A_{ff}) is defined as the point in the YBCO layer at which the internal uniaxial stress becomes zero, where the initial compressive strain decreases during tensile loading and changes to a tensile component. The A_{ff} was assessed to be about 0.19 ~ 0.21% at 77 K. A uniaxial tensile load was used to measure I_c at 77 K. I_c maximum was observed at 0.035% for the strain dependence. As a result, YBCO-coated conductors' strain at the maximum I_c does not correlate with their A_{ff}.

3.3. Raman Spectroscopy

Currently, Raman spectroscopy has been used to probe phonons and other types of low-energy excitations in HTS, which can be applied to analyze internal strains and

evaluate possible oxygen loss. For example, Sofia Favre et al. [26] deposited YBCO films by Pulsed Laser Deposition (PLD) and studied the connection between superconductivity and strain. They also studied oxygen loss effects and strain by Raman spectroscopy. The films exhibited an in-plane residual compressive strain, whose degree was determined by film thickness and growth conditions, which influenced the superconductivity. An explanation for the nearly linear depression of T_c with c-axis expansion has been proposed using mutual Coulomb screening between consecutive CuO_2 planes in the structure.

3.4. EBSD

Anjela Koblischka-Veneva et al. [27] performed a meticulous analysis of transmission Kikuchi diffraction (TKD) and electron backscatter diffraction (EBSD) data acquired on various YBCO samples doped with Y_2BaCuO_5 (Y-211) nanoparticles. The crystallographic parameter difference between Y-211 and YBCO will introduce residual strain around such embedded Y-211 nanoparticles within the YBCO matrix down to the nanometer scale. Researchers found that the strain around clusters and Y-211 nanoparticles was so large that subgrains formed in YBCO matrix. In addition, they discussed the effect of strain distribution on vortex pinning because stress or strain can provide another source of vortex pinning.

3.5. TEM

Currently, TEM has been widely applied in the field of microscale strain measurement, and the strain of various materials has been well studied. In previous research, the authors analyzed the heterointerface structure and strain of Bi-based HTS films deposited on $SrTiO_3$ [28] and MgO [29] single crystal substrates and demonstrated that the combined effect of lattice mismatch and thermal expansion mismatch caused HTS films to behave differently from the expected strain state (expected tensile strain, but actually compressive strain), as shown in Figure 3.
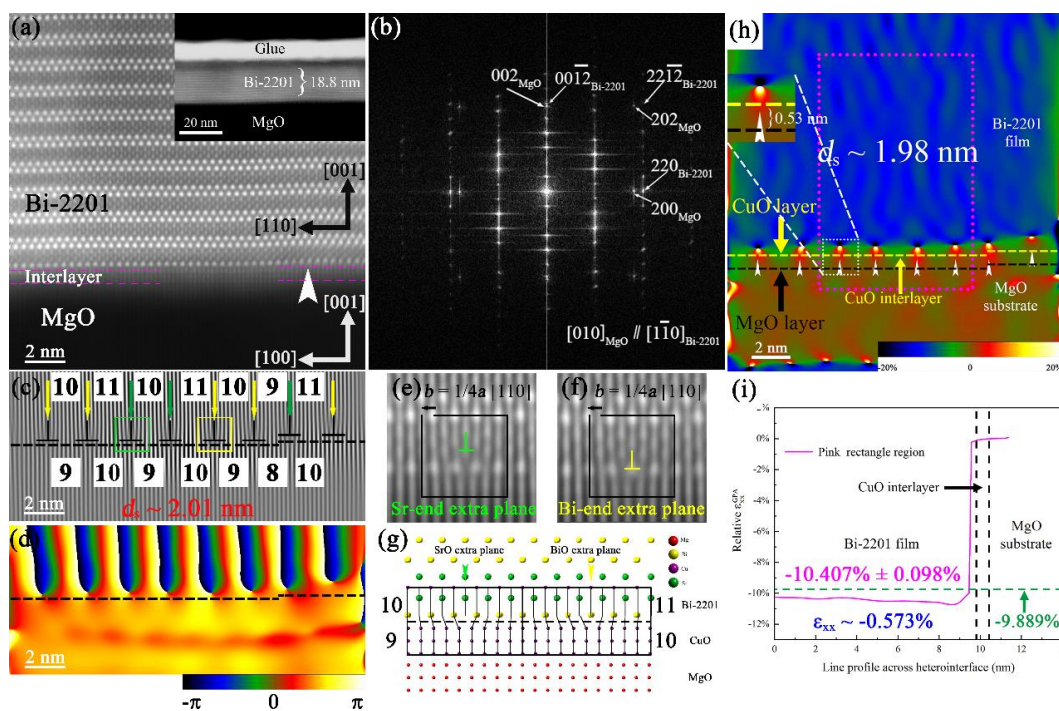

Figure 3. (**a**) HAADF image of the MgO/Bi-2201 heterointerface. (**b**) FFT image of (**a**). (**c**) (200)MgO Bragg and (**d**) geometric phase image of (**a**). Enlarged areas of the green (**e**) and yellow (**f**) squares in (**c**). (**g**) Schematic diagram of 9 or 10 (200)CuO lattices match with 10 or 11 (220)Bi-2201 lattices. (**h**) The ε_{xx} map of (**a**). (**i**) ε_{xx} along the length of the pink rectangle area in (**h**). Reprinted with permission from Ref. [29]. Copyright 2021, Elsevier.

In general, four main TEM techniques have been created to measure strain, including high-resolution (S)TEM [28–33], nanobeam electron diffraction (NBED) [34,35], convergent-beam electron diffraction (CBED) [36] and dark-field electron holography (DFEH) [37]. Strain measurements depend on their spatial resolution for precision and accuracy. As spatial resolution increases, the technique becomes less accurate. The corresponding information is shown in Table 1. For a specific discussion, see previous reviews, e.g., Martin J. Hÿtch et al. [38], David Cooper et al. [39], and A. Béché et al. [40].

Table 1. Comparison of TEM strain measurement techniques.

Technique	Precision	Spatial Resolution	Field of View	Advantages	Disadvantages
HR-(S)TEM	10^{-3}	1 ~ 2 nm	150×150 nm	High availability	Demanding specimen preparation and limited in field of view
NBED	10^{-3}	5 ~ 10 nm	—	Practical and versatile	Low spatial resolution
CBED	2×10^{-4}	0.5 ~ 2 nm	—	Most accurate technique	Easily interfered by bending atomic columns
DFEH	2×10^{-4}	2 ~ 4 nm	1500×500 nm	Largest view areas	Low spatial resolution

4. Effect of Strain on Superconducting Performance

Strain has been proved to be an efficient method of modifying superconductivity [41–43]. Experimentally, using compressive epitaxial strain, J.-P. Locquet et al. [10] doubled T_c in $La_{1.9}Sr_{0.1}CuO_4$ films, which has led to a surge in research to improve the performance of superconducting films by applying strain. In this section, we review the effect of strain on $La_{2-x}Sr_xCuO_{4+\delta}$, $Bi_2Sr_2Ca_{n-1}Cu_nO_{2n+4+\delta}$, $REBa_2Cu_3O_{7-\delta}$, and other superconducting systems. Moreover, we also focus on the effect of strain on the secondary phase vortex pinning, and the application of buffer layers to release strain.

4.1. Effect of Strain on $La_{2-x}Sr_xCuO_{4+\delta}$ System

In contrast to other cuprate superconductors, the $La_{2-x}Sr_xCuO_{4+\delta}$ (LSCO) system has a lower variation of excess oxygen content, making strain less likely to cause oxygen loss. Therefore, it is a perfect system to study the strain required to increase T_c [44–47].

I. Bozovic et al. [48] extended the work of J.-P. Locquet et al. [10] and showed that oxygen intake in such films could cause startling effects such as a crossover from semi-conductor to metallic states and colossal lattice expansion. T_c was improved to 40 K in La_2CuO_4 films deposited on $SrTiO_3$ substrates without any Sr doping and under tensile strain. On $LaSrAlO_4$ (LSAO) substrates, T_c was improved to 51.5 K, which is an excellent result for the LSCO system.

Eun-Mi Choi et al. [49] deposited self-assembled vertically aligned $La_2CuO_{4+\delta}+LaCuO_3$ nanocomposite films by PLD and observed weak signatures of superconductivity at ~ 120 K (maximum T_c ~ 40 K in bulk $La_2CuO_{4+\delta}$) by DC magnetic susceptibility measurements. The 120 K superconductivity occurred only when films contained both *a-* and *c*-axis oriented $La_2CuO_{4+\delta}$ grains. By analyzing lattice parameters close to grain boundaries, it was demonstrated that the expansion of the La perovskite block allowed grains with differently oriented orientations to interact. It is consistent with an interfacial region with a higher T_c. By strain engineering, they showed a new method for increasing the T_c in cuprate superconductors.

H. Sato et al. [50] deposited (001)-oriented $La_{2-x}Sr_xCuO_{4+\delta}$ (x = 0 ~ 2) films by reactive electron-beam co-evaporation and characterized them by XRD and resistivity measurements. By changing the *c*-axis length, they were able to obtain single-phase films for the entire range of compositions. Films (x = 0.06 ~ 0.30) with oxygen composition δ ~ 4 showed superconductivity. The T_c was maximized to 44 K for x = 0.15, owing to a strain effect caused by lattice mismatch. There was a good correlation between the film's T_c and the length of the *c*-axis. When x = 0.30, the T_c of films was strongly dependent on the residual

resistivity (ρ (0 K)), meaning they showed a higher T_c for lower ρ (0 K). When x = 0.125 was used, the depression of T_c was smaller than when it was used for bulk samples.

Under a compressive epitaxial strain, I. Zaytseva et al. [51] studied the transport properties and structure evolution of underdoped $La_{1.952}Sr_{0.048}CuO_4$ films. The films with different thicknesses (26 ~ 120 nm) were deposited. Superconductivity in films started at 26 K, but small residual resistance remained at low temperatures, suggesting a non-homogeneous state of superconductivity. There was a saturation of resistance at about 0.65 K under a perpendicular magnetic field, indicating the possible existence of a non-conventional metallic state. At a magnetic field of about 32 T, a magnetic field-tuned transition from quasi-superconductor to insulator was observed.

Yang Wang et al. [52] employed molecular beam epitaxy (MBE) to deposit LSCO films. They investigated the influence of substrate-induced strains on superconductivity and crystal parameters of LSCO films through heterointerface engineering. When deposited on $SrTiO_3$ substrates with 3% larger lattice constants than LSCO, the large tensile strain at the heterointerface prevented LSCO films' superconductivity [48]. In contrast, $LaSrAlO_4$ (LSAO) substrates had a smaller lattice constant than LSCO, which caused a slight compression at the heterointerface, which enhanced LSCO's superconductivity, as shown in Figure 4.
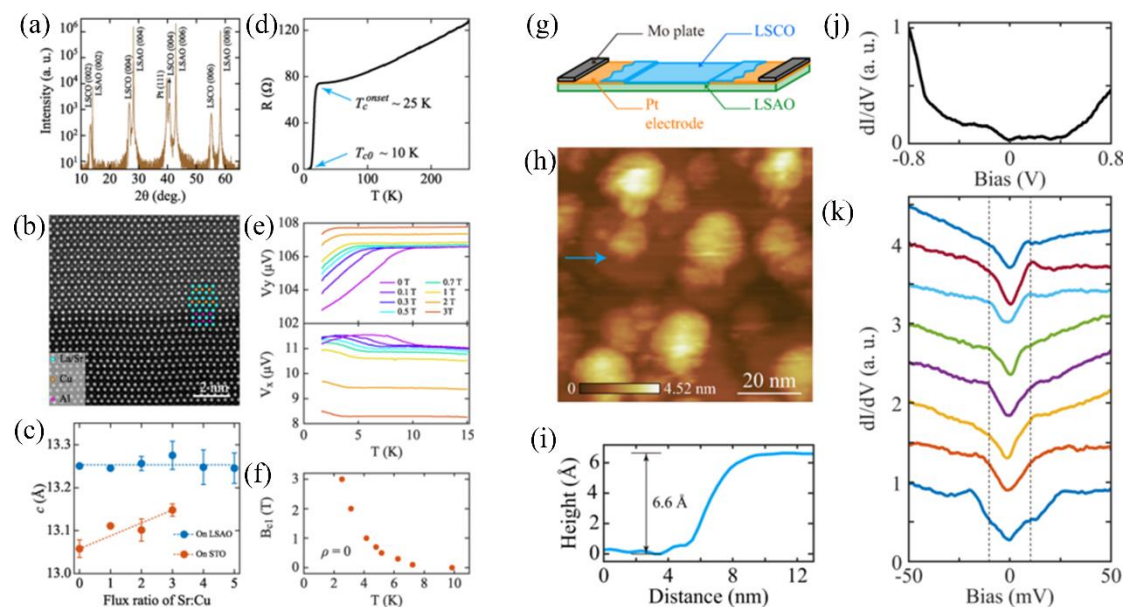

Figure 4. (**a**) XRD of the LSCO film. (**b**) STEM image of the LSCO/LSAO heterointerface. (**c**) Comparison of *c*-axis lattice parameters vs. flux ratios of Sr:Cu. (**d**) *R-T* curve of the LSCO/LSAO sample. (**e**) Imaginary and real parts of mutual inductance vs. *T* under different magnetic fields. (**f**) B_{c1} vs. *T* of LSCO films. (**g**) Schematic diagram of the LSCO film deposited on the Pt electrode pre-patterning LSAO substrate. (**h**) STM topography of the LSCO/LSAO sample. (**i**) Line profile along the blue arrow in (**h**). (**j**) Large- and (**k**) Low-energy-scale d*I*/d*V* spectrum in the LSCO/LSAO film. Adapted with permission from Ref. [52]. Copyright 2021, American Chemical Society.

X. Zhang et al. [53] characterized interstitial oxygen atoms in $La_2CuO_{4+\delta}$ by integrated differential phase contrast scanning transmission electron microscopy (iDPC-STEM) technique as shown in Figure 5. The interstitial oxygen atoms in $La_2CuO_{4+\delta}$ lay in $La_2O_{2+\delta}$ layers and their distribution was sensitive to local strain states and could be modulated by strain. High in-plane stress in $La_2CuO_{4+\delta}$ created periodic oscillations in La-O layers between compressive and tensile strain. Rather than being randomly distributed, mobile interstitial oxygen atoms self-organized to form oxygen-depleted stripes which are divided by ordered oxygen interstitials. In addition, density-functional-theory (DFT) calculations revealed local changes in electronic and atomic structures. Dopant oxygen atoms could

be adapted in CuO_6 octahedrons by shifting surrounding atoms and distorting CuO_6 octahedras. The interaction between CuO_6 octahedras and dopant oxygen atoms induced charge transfer from LaO planes (charge carrier reservoir) to CuO_2 planes (hole doping). By forming apical O of CuO_6 octahedra, oxygen atoms in LaO planes created a link between O and CuO_2 planes, increasing the hole carrier concentration of CuO_2 planes. Their result offered a systematic view of the locations of dopant O atoms and their impact on the electronic and atomic structure of $La_2CuO_{4+\delta}$.
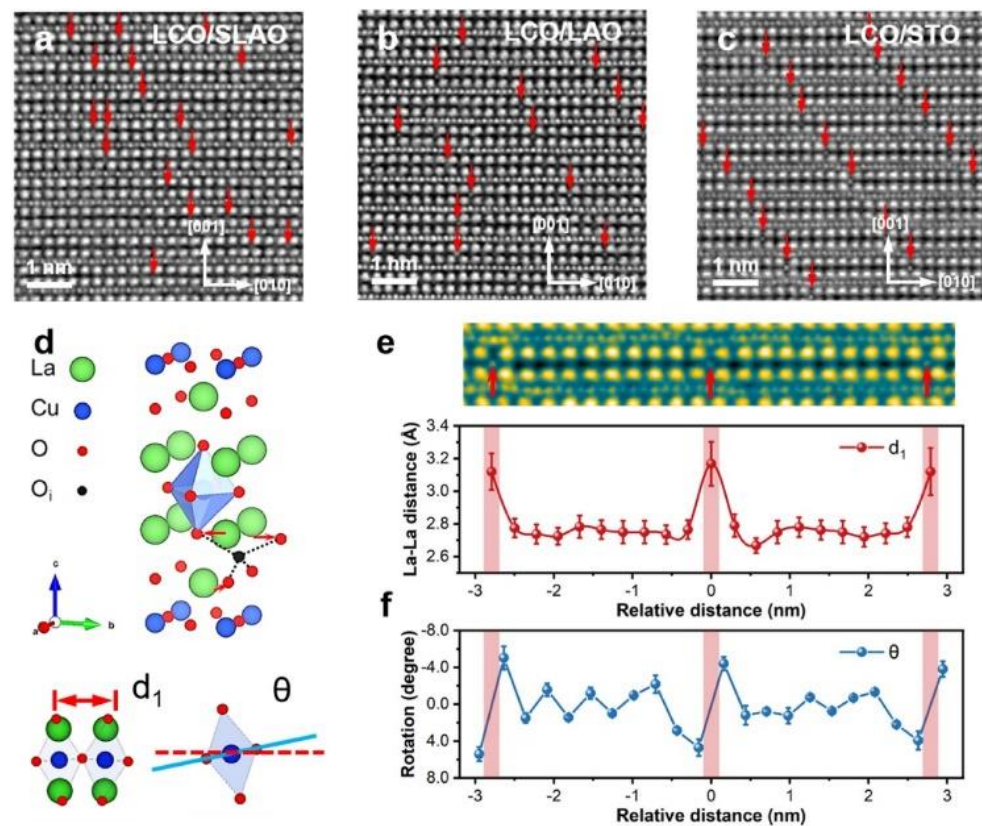

Figure 5. iDPC-STEM micrograph of $La_2CuO_{4+\delta}$ deposited on (**a**) SLAO, (**b**) LAO, and (**c**) STO substrates, respectively. Red arrows illustrate the interstitial oxygen atomic columns. (**d**) Schematic structure of $La_2CuO_{4+\delta}$. Only half of the orthorhombic cell is presented. The interstitial oxygen can lead to the slight shift of La and apical oxygen and the CuO_6 octahedra tilted. (**e**) The distance (d_1) of La–La atomic column spacing and (**f**) the rotation of the CuO_6 octahedra along the *b* axis vs. the relative distance from the interstitial oxygen. Reprinted with permission from Ref. [53]. Copyright 2022, Elsevier.

4.2. Effect of Strain on $Bi_2Sr_2Ca_{n-1}Cu_nO_{2n+4+\delta}$ System

$Bi_2Sr_2Ca_nCu_{n-1}O_{2n+4+\delta}$ has intrinsic strain due to its structural complexity, which is especially suitable for strain study of superconductors. The largest source of strain in $Bi_2Sr_2CaCu_2O_{8+\delta}$ (Bi-2212) is the incommensurate structural buckling (a mismatch between rock-salt BiO_2 layers and CuO_2 planes) called "super-modulation" with a period of ~26 Å, oriented at 45° from the Cu-O bond [54,55]. The second source is a commensurate orthorhombic distortion that shifts two sublattices in opposite directions primarily in BiO planes, perpendicular to the super-modulation wavevector [56,57]. In both modulations, oxygen atoms in the lattice are distorted by more than 0.5 Å.

Bennie ten Haken et al. [58] investigated the mono and multifilamentary Bi-2212 wires in the Ag matrix by an axial strain experiment. A tensile or compressive axial strain was achieved by soldering superconducting samples to a bent substrate. In magnetic fields up to 16 T at 4.2 K, the I_c-strain dependence was measured with strains ranging from −2% to +1.2%. All strain-induced reductions in I_c in Bi-2122 samples were irreversible. Moreover,

the strain change did not result in a significant rise in I_c. A special emphasis was placed on axial strains in the tensile regime (0 ~ 0.4%). In this case, I_c was reduced slightly but significantly. This strain behavior indicated that fractures in superconducting filaments are responsible for the I_c reduction.

The electronic inhomogeneity of HTSs may provide an opportunity to enhance superconducting pairing. Ilija Zeljkovic et al. [8] reported the correlation between local strain and regional doping in Bi-2212. Scanning tunneling microscopy (STM) revealed periodic distributions of oxygen dopants related to local strain. By investigating all oxygen dopant positions, they provided crucial structural input for a complete microscopic theory.

Prapaiwan Sunwong et al. [59] investigated the impact of magnitude and direction of magnetic field on BSCCO tapes under tensile and compressive strains. The anisotropy, texture and structure of $Bi_2Sr_2Ca_2Cu_3O_{10+\delta}$ (Bi-2223) had a great influence on J_c. The magnitude and angle correlations with J_c are shown in Figure 6 and could be explained by a simple anisotropic exponential magnetic field model that contained the influence of 2D and grain misalignment. In the range of reversible strain, the variation in normalized was linear, where temperature and field were not relevant to the gradient of strain dependence. Degradation by compression extended the reversibility further into the compressive regime.
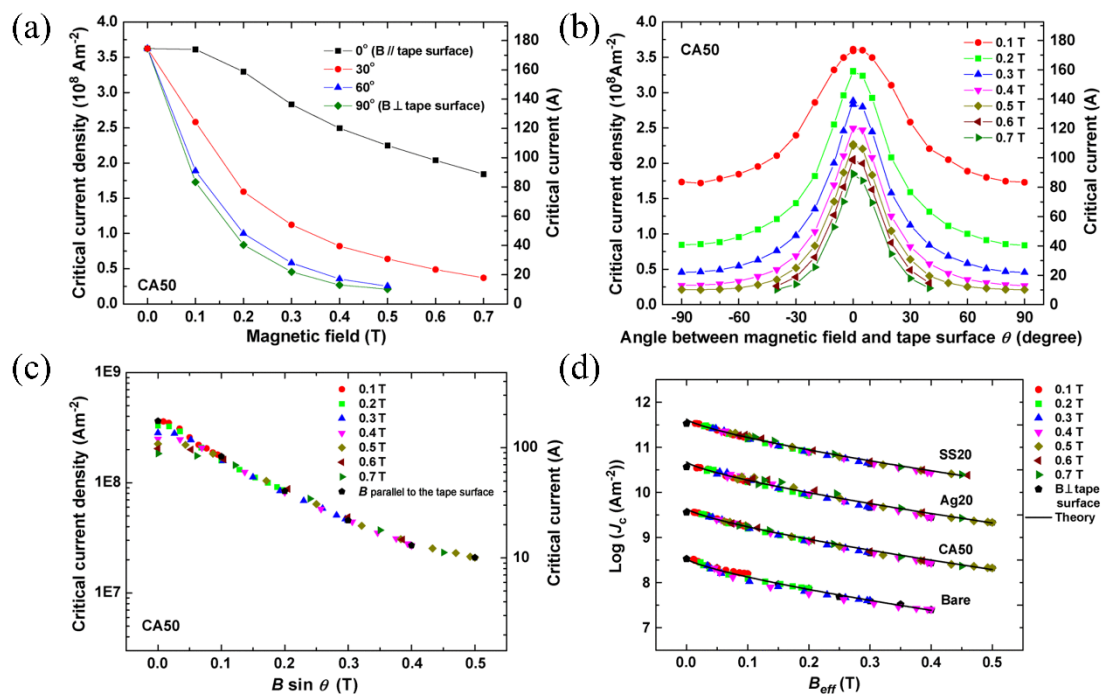

Figure 6. The electrical transport properties of the BSCCO tape at 77 K. (**a**) J_c vs. B for different field orientations. (**b**) J_c vs. θ at different applied magnetic fields. (**c**) I_c vs. $B\sin\theta$ of the tape. (**d**) J_c vs. B_{eff} for different tapes at 77 K. Reprinted with permission from Ref. [59]. Copyright 2011, IEEE-Inst Electrical Electronics Engineers Inc.

L. Forro et al. [60] measured the in-plane resistivity (ρ_{ab}) and out-of-plane resistivity (ρ_c) of Bi-2212 single crystals under pressure ~20 kbar. ρ_{ab} had an initial derivative, $d(\ln\rho_{ab})/dP = -0.75\%$ /kbar. However, the effects of pressure were much greater on ρ_c, $d(\ln\rho_{ab})/dP = -4.0\%$ /kbar. Throughout the pressure range covered, T_c increased monotonically by +0.15 K/kbar in all configurations.

S. Klotz et al. [61] studied the relationship between T_c and the pressure of Bi-2212 single crystals. The dependence of T_c of Bi-2212 single crystals on hydrostatic pressure to 7 GPa was measured at three different oxygen concentrations. All three cases showed markedly nonlinear $T_c(P)$ behavior. With increasing oxygen concentrations, $dT_c/dP = +1.2$ K/GPa for the samples with $T_c(0) = 80$ K and 88 K, followed by maximum in $T_c(P)$ measurements at 4 GPa and 1.5 GPa for the samples, respectively. When the oxygen-poor sample

was exposed to 1.5 GPa, $T_c(0)$ did not change much. At higher pressure, $T_c(0)$ showed a downward trend, but the decrease was slow. In the absence of a pressure medium, when the anvils directly contacted the sample, $T_c(P)$ exhibited a markedly different pressure dependence. Models based on charge transfer cannot account for the present results.

Xiao-Jia Chen et al. [62] studied the pressure dependence of T_c up to 18 GPa of Bi-2212 single crystals with underdoped, optimally doped, and overdoped levels. For all samples, as pressure increases, T_c increased initially and saturated at critical pressure (P_c) subsequently. As pressure increased, T_c decreased modestly. Oxygen doping tends to decrease the increase in P_c and T_c. It was then possible to construct a high-pressure phase diagram between saturated P_c and T_c. A theoretical interpretation, according to the competition between pairing interaction strength and hole carrier density, was given based on transport data of the Hall coefficient and the resistivity in this system.

Dongsheng Song et al. [63] observed the locations of dopant oxygen in Bi-2212 by the HAADF-STEM and iDPC-STEM techniques, as shown in Figure 7. According to iDPC and DFT results, the favorable positions of dopant oxygen between SrO and BiO can be explained by local strain analysis. Furthermore, the DFT calculations revealed local changes in electronic and atomic structure. As the surrounding atoms shift, dopant O atoms were accommodated, further aggravating the distortions. At the same time, the dopant O atoms induced charge transfer from BiO planes (charge carrier reservoir) to CuO_2 planes (hole doping). The O atoms of SrO planes served as apical O in CuO_5 pyramids, establishing a correlation between the dopant O and CuO_2 planes, and improving hole carrier concentration. Their work provided an in-depth insight into the dopant oxygen atom locations and how dopant O atoms affect the electronic and atomic structure of Bi-2212.
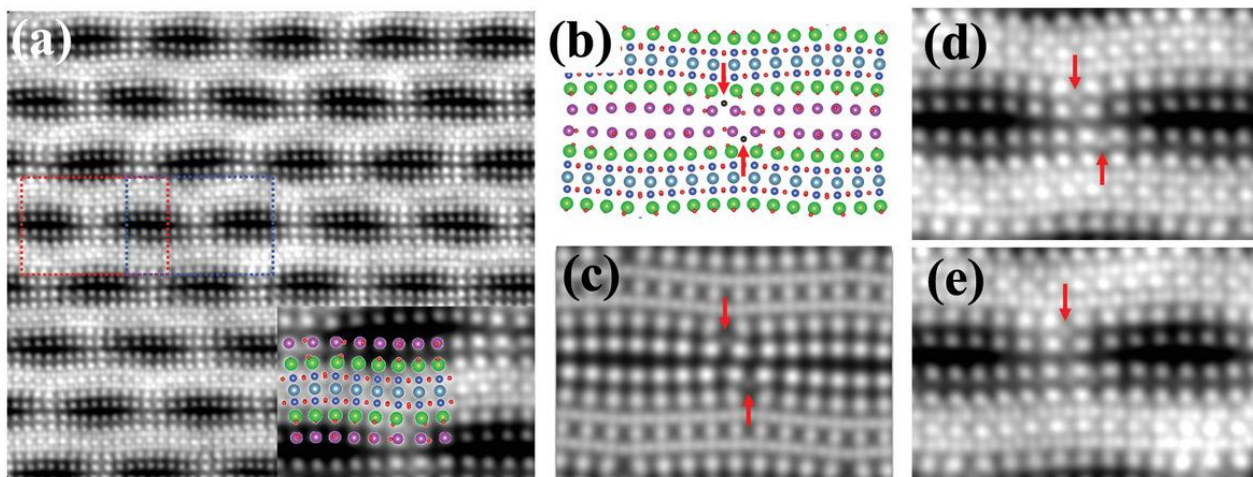

Figure 7. Imaging of dopant oxygen atoms. (**a**) iDPC-STEM image of Bi-2212 along *b*-axis. (**b**) Schematic diagram of Bi-2212. (**c**) Simulated iDPC-STEM image. Enlarged images taken from the dotted red (**d**) and blue (**e**) rectangles in (**a**). Reprinted with permission from Ref. [63]. Copyright 2019, Wiley.

4.3. Effect of Strain on the $REBa_2Cu_3O_{7-\delta}$ System

In YBCO's unit cell structure, CuO_2 planes are separated by oxygen-free Y layers. CuO_2 planes are linked to Cu-O chain layers oriented along the *b*-axis by a bridging or apical O referred to as O(4) in Figure 8. Thus, orthorhombic YBCO contains five inequivalent oxygen sites.

D. C. van der Laan and J. W. Ekin et al. [65] measured the intrinsic effect of axial strain in YBCO-coated conductors. YBCO for electric power applications has been measured in a wide spectrum of strains with a new technique to demonstrate a significant reversible reduction in critical current (I_c). I_c was reduced by 40% at 1% compressive strain in the self-magnetic field, and this effect was symmetric for tensile and compressive strains.

A significant impact is expected from this effect and its magnitude on power applications. It can offer a new idea for exploring the basic properties of current transport in HTSs.
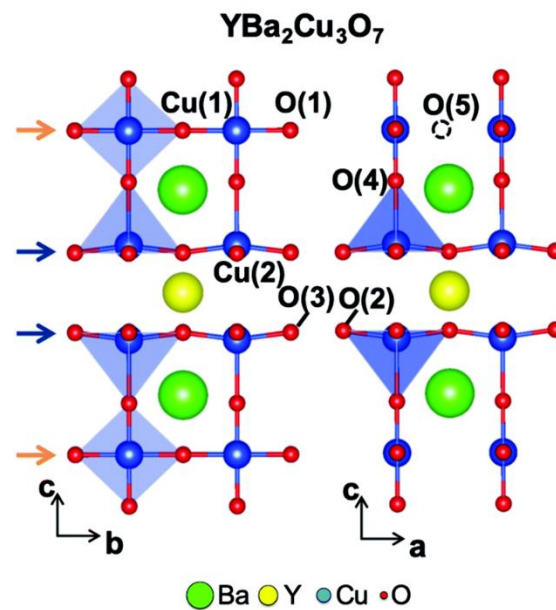

Figure 8. Schematic diagram of the YBCO unit cell. Reprinted with permission from Ref. [64]. Copyright 2020, Royal Society of Chemistry.

N. Cheggour and J. W. Ekin et al. [15] studied the impact of axial strain on J_c for YBCO coatings on different substrates. According to their study, the reversible degradation of J_c occurred at about twice the substrate's yield strain. Axial-strain performance requirements of electric devices, such as motors and generators, requiring strain tolerances exceeding 0.25%, can be met by YBCO/Ni-alloy composites. Furthermore, the YBCO/Ni-5-at.%-W conductors exhibited a reversible strain effect, which may be induced by a reversible strain-field broadening around mismatch dislocations at grain boundaries.

Through finite element analysis, Barth et al. [66] studied the effect of twisting or torsion exerted on HTS tapes as a source of longitudinal and shear stress. Van der Laan et al. [67] reported that the strain fields surrounding grain boundary dislocations in YBCO thin films significantly suppressed the local J_c. J_c increased dramatically when strain was removed from superconducting grain boundary channels by compressive strain. Grain boundary channels have strain-free J_c values comparable to intrinsic J_c values of grains.

R. Guzaman et al. [68] systematically studied the local strain distribution within YBCO films. By forming Y124, strain-derived interactions with other defects were concatenated and intrinsic defects were nucleated in YBCO films, resulting in a distributed network of randomly distributed nanostrained regions that profoundly altered vortex-pinning efficiency.

K. N. Yugay and A. V. Muravjev [69] used laser ablation to deposit strained YBCO films (thicker than the critical thickness) on $LaAlO_3(100)$ substrates. By rapidly cooling films after deposition, strains were frozen in films. Unusual temperature dependence of J_c was observed in these films: a characteristic minimum was observed between 55 ~ 57 K. The J_c decreased from 10^6 A/cm^2 to 10^4 A/cm^2 and was lower at 77 K. The films are stable against thermocycling from 300 K to 77 K. STM analysis showed that strain domains were formed in films, leading to a macroscopic structural organization. On average, as the strain increased, the size of domains decreased, from 2.4 to 1 μm. Magnetic fields penetrated differently into strained films than into single-crystal or granular films, which implied that the films had a macroscopic structure.

Based on X-ray diffraction line broadening, X. Obradors et al. [70] discovered that J_c and YBCO films' mesostrain were adversely correlated. Mesostrain was enhanced when grain boundaries were not effectively healed, for example by shortening annealing times or

lowering growth temperatures. By applying the bond contraction pairing model to strained regions at low angle grain boundaries, the microscopically observed weak link behavior could be explained by pair formation prevention.

Using epitaxial YBCO films on (001)-oriented piezoelectric $Pb(Mg_{1/3}Nb_{2/3})_{0.72}Ti_{0.28}O_3$ substrates, P. Pahlke et al. [71] applied reversible and continuous biaxial strain to underdoped and optimally doped YBCO films. With an electric field applied to the substrates, the biaxial strain (~0.1%) was able to be induced into YBCO films, which resulted in a reversible and continuous shift in T_c, the upper critical field, and the normal state resistance. YBCO films with optimal doping had a shift of T_c of 0.75 K per 1% compressive biaxial strain, whereas underdoped films had a shift of 4.20 K. These values matched highly with strain sensitivity data calculated from pressure experiments.

D C van der Laan et al. [21] found that YBCO-coated conductors with axial strain underwent a large, magnetic-field-dependent, reversible reduction in J_c at 75.9 K. This effect could be potentially significant in applications where YBCO coatings were subjected to high stresses and magnetic fields. Scientists constructed a device to measure J_c as a function of axial tensile and compressive strains and applied magnetic fields to determine its magnitude and origin. At all magnetic field angles, J_c reduced reversibly with strain increasing. When 8 T magnetic field was parallel to *ab*-plane of the conductor or 5 T to *c*-axis, J_c was reduced by about 30% at 0.5% strain, compared with about 13% reduction in self-field at 76 K. Different J_c strain responses at various magnetic field angles revealed that strain was uniquely affecting the pinning mechanism in YBCO-coated conductors.

D. Putzky et al. [72] utilized atomic layer-by-layer MBE (ALL-MBE) to synthesize $DyBa_2Cu_3O_{7-d}$ films with minimal defect density. Orthorhombic and tetragonal structures with different twinning patterns were revealed by X-ray reciprocal-space maps. They elucidated the evolution of oxygenation state, film thickness, and epitaxial relationship with substrates. In addition, they found that films with a higher degree of orthorhombicity exhibited higher T_c and lower normal-state resistivities. Consequently, optimized superconducting heterostructures and devices can be synthesized based on these findings.

The strain effect on I_c in YBCO coated conductors at 20–83 K under magnetic fields parallel to *c*-axis up to 10 T was investigated by Michinaka Sugano et al. [13], as shown in Figure 9. Across all tested temperatures, I_c exhibited reversible peak variation in self-field with applied uniaxial strain. As the temperature increased, strain sensitivity increased, which resulted in a more obvious reversible suppression with strain. In a fascinating finding, as the temperature decreased, the peak strain corresponding to I_c's maximum shifted to the compressive side. I_c's peak strain cannot be explained by changes in the residual thermal strain of YBCO films alone, as this peak shift cannot be explicated by the relaxation of residual strain. At 60 K, I_c strain sensitivity increased with the increasing magnetic field, whereas at 20 K, magnetic field influence was less pronounced. When the magnetic field was low, at 77 and 83 K, the in-field I_c displayed a double peak behavior both at compressive and tensile regions.

It is well known that in YBCO, oxygen vacancies (V_Os) regulate the carrier concentration, J_c and T_c. Bernat Mundet et al. [64] demonstrated that V_O accommodated local strain fields caused by large-scale crystal defects. A significant influence on the location and concentration of V_O was found to be related to nanoscale strain relevant to $Y_2Ba_4Cu_8O_{16}$ (Y248) intergrowths. Based on DFT calculations and local probe measurements, it appears that strain caused the V_O to reorder from CuO chains into the bridging apical sites in BaO planes, where it bound directly to superconducting CuO_2 planes. Their results have strong connotations on the physical properties of YBCO, because apical V_Os altered carriers transfer to CuO_2 planes, which is identified by electron energy loss spectroscopy (EELS), and created structural changes. Further, the discovery of apical V_Os also had an influence on regulating J_c and enhancing the vortex pinning process.
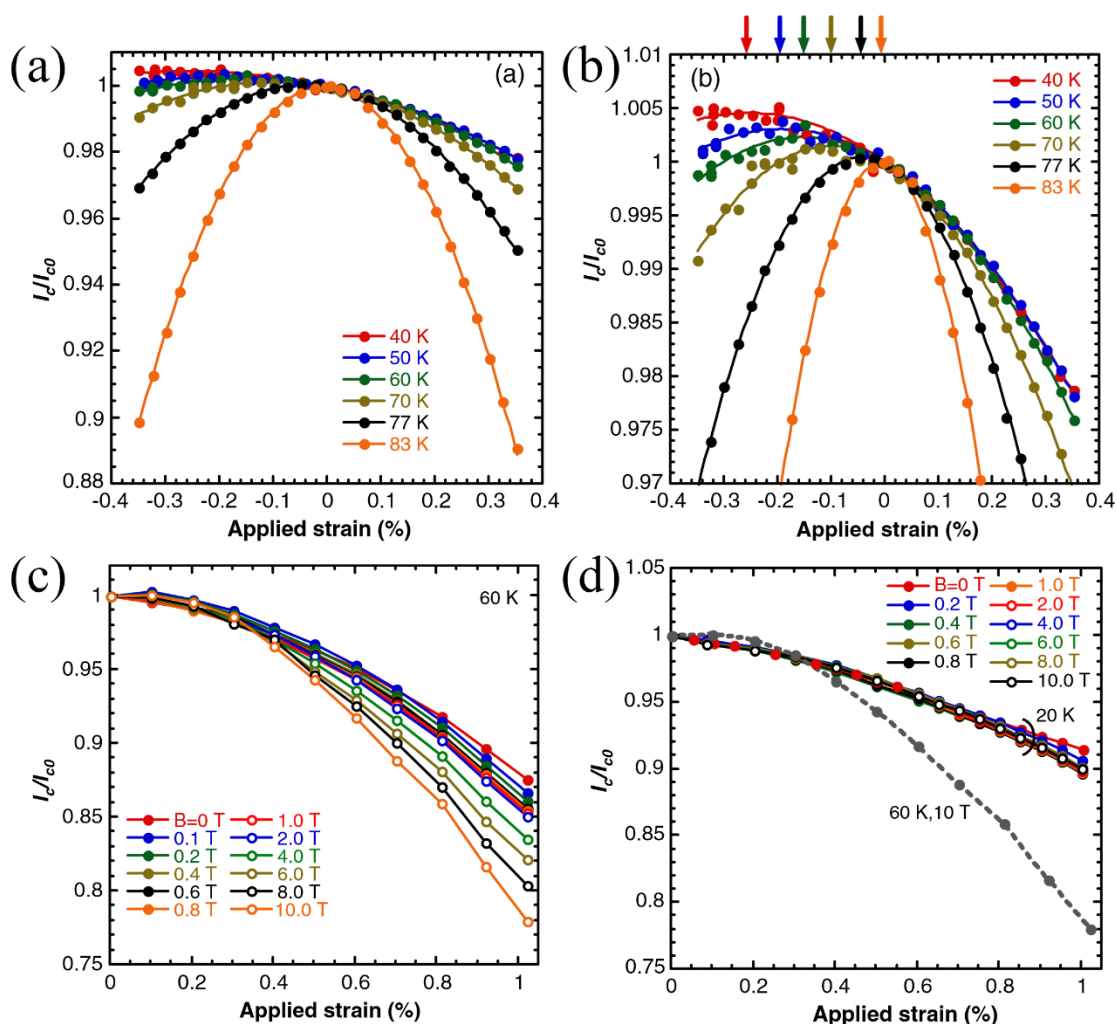
Figure 9. *T* vs. normalized I_c in self-field for 0.1 µm thick YBCO layers. The whole data (**a**) and corresponding enlarged view (**b**) around the peak are presented. *B* vs. normalized I_c at 60 K (**c**) and 20 K (**d**). Reprinted with permission from Ref. [13]. Copyright 2010, IOP Publishing Ltd.

4.4. Effect of Strain on Other Superconductor Systems

Alongside cuprate superconductors, lattice strain is also important in other types of superconductors. For example, in FeSe system, T_c was enhanced by growing epitaxial thin films on $SrTiO_3$ substrates (from 8 K for bulk material to above 65 K) [73–75]. Both electronic structure reconstruction and biaxial lattice strain seemed to have an influence on improving T_c by charge transfer from oxygen-vacancy-induced states of substrates.

S. J. Zhang et al. [76] measured the resistance of Li_xFeAs (x = 0.8, 1.0, 1.1) superconductors under high pressure. It is found that T_c decreased almost linearly with the increase in pressure and pressure derivative (dT_c/dP). In situ synchrotron radiation powder, X-ray diffraction experiments at high pressure demonstrated no correlation between structural transitions and resistivity.

Under uniaxial compressive stress, Ekin [77] observed a large reversible degradation of I_c in Nb_3Sn [77]. In addition, Ekin [77,78] also studied the H_{C1} under transverse compression stresses. H_{C1} of Nb_3Sn was intrinsically affected by transverse stress ten times more than by axial stress. Further investigations of the strain's influence on H_{C1} have been published in recent papers [79–81].

A.V. Pogrebnyakov and J. M. Redwing [82] reported that tensile strain led to a remarkable increase in T_c in MgB_2 films, which was well beyond the bulk value. Due to the coalescence of initially nucleated discrete islands, tensile strain increased with increasing

MgB_2 film thickness. On sapphire and SiC substrates, epitaxial films showed T_c increases, but the values for the two types of substrates differed due to lattice mismatch and thermal expansion mismatch. According to first-principles calculations, the increase in T_c is due to a softening of the bond-stretching E_{2g} phonon mode, which is defined by Raman scattering. According to their results, E_{2g} phonon softening was an option for achieving higher T_c with MgB_2-related materials.

Y. C. Liu et al. [83] investigated the superconductivity of Sr_2RuO_4 films under strain. Their experiments showed that tensile strain caused charge transfer to the γ-band and consequent Lifshitz reconstruction of the Fermi surface. According to theoretical calculations, a *p*-wave superconducting order was realized with enhanced T_c within a limited range of tensile strain. With an increase in strain, however, before reaching the Lifshitz transition, the system had developed into the spin-density wave (SDW) state. They also considered the effect of compressive strains. A transition from the *p*-wave SC state to the nodal *s*-wave SC state occurs as strain increases. A comparison of theoretical results to the experiment can be made, and further experiments can be performed to verify the results. As biaxial strain played a vital role in modulating the system to Van Hove filling, they predicted that T_c may also rise rapidly on a fixed substrate but the thin film is slightly gated toward higher filling.

It has been several decades since $SrTiO_3$, the first oxide superconductor was discovered, but its nature of superconductivity remains a source of intense debate. Recent theoretical studies have implied the incipient ferroelectric properties and superconductivity of $SrTiO_3$ may be linked. K. Ahadi [84] studied the phenomenon of enhanced superconductivity of $SrTiO_3$ films under strain state. They grew strained, epitaxial $SrTiO_3$ films, which underwent ferroelectric transitions, to test whether such a connection exists. Within a range of carrier densities, when compared with unstrained films deposited under the same conditions, T_c was enhanced by up to a factor of two. Additionally, superconductivity emerged from a resistive state in these films. Localization behavior was discussed in the context of ferroelectricity proximity. The results provided new chances to enhance T_c in oxide materials.

Through calculation, Mano et al. [85] found that Li-doped MoS_2 thin films performed differently in tensile and compression states, which was believed to result from the change in topology structure of the Brillouin region on the Fermi surface and the increase in electron-phonon matrix elements. Using ab initio calculations, they showed that tensile or compressive strain could enhance the superconductivity of Li-intercalated bilayer MoS_2. It was found that the mechanism of superconductivity enhancement differed for tensile strains and compressive strains. In a large range of Brillouin zones, it was possible to explain enhanced electron-phonon coupling (EPC) under tensile strain as a result of a change in Fermi surface topology, increasing the nesting function. When 6.0% tensile strain was applied, the T_c of 0.46 K at zero strain increased to 9.12 K. Moreover, increased intrinsic electron-phonon matrix elements can explain the enhancement under compressive strain. Additionally, electron pockets on Fermi surfaces played a significant role in interband scattering. Finally, approximately 80% of the overall EPC (λ = 0.98) originated from these pockets and the T_c was estimated at 13.50 K.

4.5. Effect of Strain on Secondary Phase Vortex Pinning

In high-T_c cuprate superconductors, lattice distortion can modify pairing, resulting in enhanced vortex pinning due to nanostrain. Hence, a comprehensive insight into the strain landscape is necessary for large-scale HTS applications. However, identifying defects' type and distribution, along with associated strain, is crucial work.

A. Llordés et al. [86] demonstrated a highly effective artificial pinning centers (APCs) mechanism in HTS nanocomposite films by generating nanostrained regions which suppressed the formation of Cooper pair formation. Nanostrained regions characterized by TEM revealed highly concentrated dislocations relevant to intergrowths between epitaxial YBCO matrix and randomly oriented APCs, as shown in Figure 10a–d. Randomly ori-

ented oxide nanoparticles caused nanoscale defects to occur in YBCO matrix, especially $YBa_2Cu_4O_8$ (Y248) intergrowths (extra Cu-O chains), which eventually resulted in highly localized strained areas where Cooper pair formation was suppressed [86,87]. Consequently, the nanostrain significantly enhanced vortex pinning in randomly oriented APCs. By quenching Copper pair formation under tensile strain, a new and effective vortex pinning mechanism was proposed based on the bond contraction pairing model, as shown in Figure 10e–i.
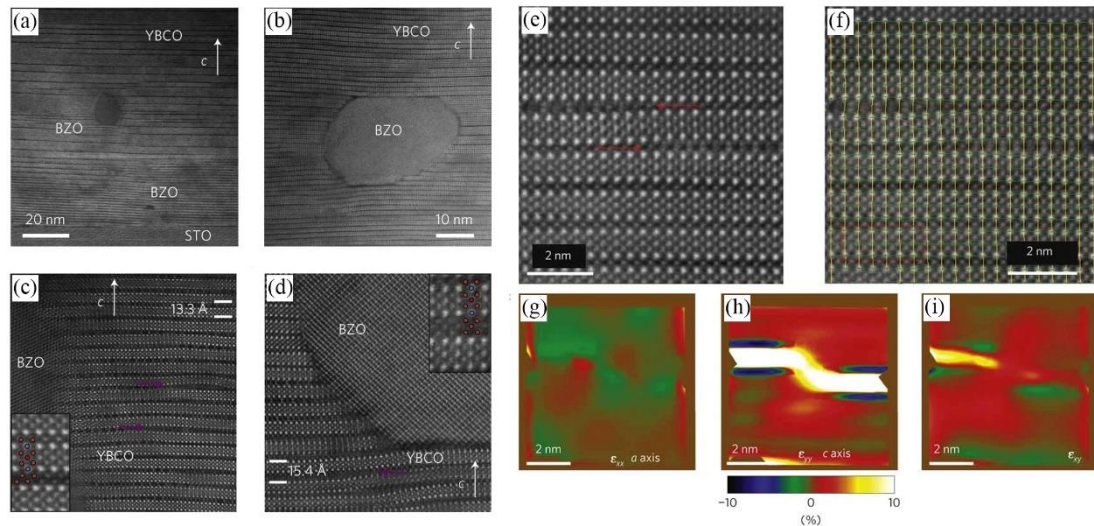

Figure 10. Z-contrast images of BZO nanoparticles in YBCO matrix at low (**a**) and high (**b**) magnification. (**c**,**d**) High-resolution Z-contrast images present the region between two different BZO nanoparticles. The insets in (**c**,**d**) show intergrowth in detail. (**e**) Z-contrast image where the strain maps were generated. (**f**) Grid obtained by Peak Pairs Analysis (PPA) from (**e**). (**g**–**i**) ε_{xx}, ε_{yy} and ε_{xy} maps, respectively. Reprinted with permission from Ref. [86]. Copyright 2012, Nature Portfolio.

Pablo Cayado et al. [88] utilized the CSD method to deposit $GdBa_2Cu_3O_{7-d}$ (GdBCO) and GdBCO–Gd_2O_3 nanocomposite films. The structural and physical properties of GdBCO films were remarkable, presenting an (*00l*) epitaxial orientation, with T_c values achieving 92.8 K, which was an increase of more than 1 K over standard YBCO films. As a result of the presence of Gd_2O_3 nanoparticles, nanostrain values reached 0.24 ± 0.01% in GdBCO–Gd_2O_3 nanocomposite films, higher than those of GdBCO-low fluorine films (0.13 ± 0.01%). Aside from that, the nanostrain obtained in GdBCO–Gd_2O_3 nanocomposite films was comparable with that found in CSD YBCO nanocomposites.

Roger Guzman et al. [68] applied scanning transmission electron microscopy (STEM) to analyze the microstructure of individual defects in YBCO nanocomposite films. Due to the introduction of incoherent secondary phase nanoparticles, the density of $Y_1Ba_2Cu_4O_8$ (Y124) intergrowths increased significantly. It has been shown that the formation of Y124 triggered strain-induced interactions with other defects as well as intrinsic defect nucleation. These interactions resulted in a net of randomly distributed nanostrained regions, transforming the vortex pinning landscape profoundly. It is believed that the additional structural strain, triggered by nanoparticles and corresponding induced defects, enhanced the vortex pinning [89].

It is well known that $BaMO_3$ (B*M*O, *M* = Zr, Hf, Sn, etc.) self-organizes into nanocolumns in *RE*BCO films deposited by vapor phase epitaxy. C. Cantoni et al. [90] reported that oxygen defects were induced at the contact surface between $BaZrO_3$ and YBCO matrix due to strain, leading to a strong vortex pinning effect, and thus, significantly increasing J_c of YBCO superconductors. A higher concentration of $BaZrO_3$ nanocolumns results in a larger entire tensile strain of the *RE*BCO along the *c*-axis, causing an average increase in *c*-axis lattice parameter.

Jiachao Ye et al. [91] prepared 1 mol% and 3 mol% of BaHfO$_3$-doped Y$_{0.5}$Gd$_{0.5}$Ba$_2$Cu$_3$O$_{7-\delta}$ (YGdBCO) nanocomposite films with a micron level thickness on CeO$_2$ layers under different laser fluences respectively by PLD. Under a higher laser fluence, compared with 1 mol% films, 3 mol% of BaHfO$_3$-doped YGdBCO films had lower self-field J_c at 77 K, dropping from 2.143 to 1.75 MA/cm^2, even though there was a smoother surface. When the laser fluence was lower, both films had poorer surface morphology and superconductivity, which could be explained by the appearance of *a*-axis-oriented grains and disordered nanoparticles on the surface attributed to reduced diffusion energy. Moreover, the superconductivity decreased with increasing BaHfO$_3$ doping concentrations. As a result of lattice mismatch, strain fields would further reduce diffusion energies of YGdBCO atoms, making it easier to form *a*-axis-oriented grains and degradation of surface quality, thereby aggravating the reduction in I_c.

S Miura et al. [92] fabricated BaHfO$_3$-doped SmBa$_2$Cu$_3$O$_y$ (SmBCO) nanocomposite films via PLD with the low-temperature growth (LTG) technique. With the LTG technique, high-quality SmBCO films can be fabricated at low substrate temperatures during deposition, and BaHfO$_3$ nanocolumn density can be greatly increased. By TEM observations, they identified that 5.6 vol% BaHfO$_3$-SmBCO films had a high density [(4.8 $\pm$ 0.3) $\times$ 10^3 μm^{-2}] of pony-size (5.4 $\pm$ 0.7 nm) BaHfO$_3$ nanocolumns. In 9 T, maximum flux pinning force (F_p) was 405 GN m^{-3} for 40 K and 105 GN m^{-3} for 65 K. It is believed that the small size and high density of nanocolumns in SmBCO matrix can enhance F_p at low temperatures under a high magnetic field. Subsequently, Yusuke Ichino et al. [93] deposited SmBCO films with 16 vol% BaHfO$_3$ using PLD and LTG techniques. As compared with 5.6 vol% BaHfO$_3$-doped samples, BaHfO$_3$ nanocolumns had a higher number density and a smaller diameter. Due to the substantial BaHfO$_3$ content, conventional X-ray diffraction could readily evaluate the lattice strain exerted on SmBCO and BaHfO$_3$. Based on this evaluation, the tensile strain on SmBCO decreased with decreasing substrate temperature, whereas the compressive strain on BaHfO$_3$ increased. Results suggested that *RE*BCO was not significantly influenced by narrow nanocolumns exerting stress. Due to the small amount of stress induced by B*M*O nanocolumns, LTG proved to be an efficient method for preparing *RE*BCO films with high-density B*M*O nanocolumns.

S V Samoilenkov et al. [94] performed accurate X-ray diffraction studies on BaZrO$_3$, BaCeO$_3$ and Y$_2$O$_3$ doped epitaxial YBCO nanocomposite films. It was found that all of the introduced secondary phases were expanded within the *ab*-plane and compressed along the *c*-axis. The tetragonal distortion increase was observed in the row BaZrO$_3$-BaCeO$_3$-Y$_2$O$_3$. In the post-deposition oxygenation step, the *c*-axis lattice parameter of YBCO decreased abnormally large, resulting in anisotropic strains. This suggestion was supported by experimental observations on reoxygenated and reduced samples. As the oxygen content of YBCO changes, nanoinclusions' strain appeared to be reversible.

Tomoya Horide et al. [95] fabricated BaZrO$_3$, BaSnO$_3$, and BaHfO$_3$-doped YBCO nanocomposite films on SrTiO$_3$(100) substrates by PLD. Their work characterized and modeled the highly elastically strained nanocolumns, the heterointerface region with dislocations and distortion, as well as the matrix with oxygen vacancies induced by strain, as shown in Figure 11a. Large misfit strains were elastically accommodated by nanocolumns so the concentration of oxygen vacancies was small enough for YBCO to maintain high T_c (>85 K). The microstructure of YBCO was distorted by the interfacial bonding distorted; however, the distortion thickness was limited to several unit cells (less than coherence length) because of the electron screening. In nanocomposites, the influence of volume fraction on electron screening and the elastic strain was critical for strong vortex pinning without significant degradation of F_p and T_c, as shown in Figure 11b–d.

Masaya Gondo et al. [96] deposited double perovskite Ba$_2$LuNbO$_6$(BLNO) doped YBCO films on SrTiO$_3$ substrates by PLD, and corresponding nanostructures were characterized by TEM and STEM. By cross-sectional observations and elemental mapping, it has been demonstrated that BLNO was self-assembled, resulting in nanocolumns stretching straight from the substrate to the surface of YBCO films. The formation of BLNO

nanocolumns was disturbed by stacking faults perpendicular to the growth direction. GPA strain maps showed that tensile strain occurred around BLNO nanorods in the YBCO matrix. At the heterointerface between the nanocolumns and matrix, misfit dislocations were periodically introduced, resulting in inhomogeneous strains of YBCO around BLNO nanocolumns. To determine their superconducting properties, YBCO nanocomposite films with normal and double perovskite nanocolumns were compared.
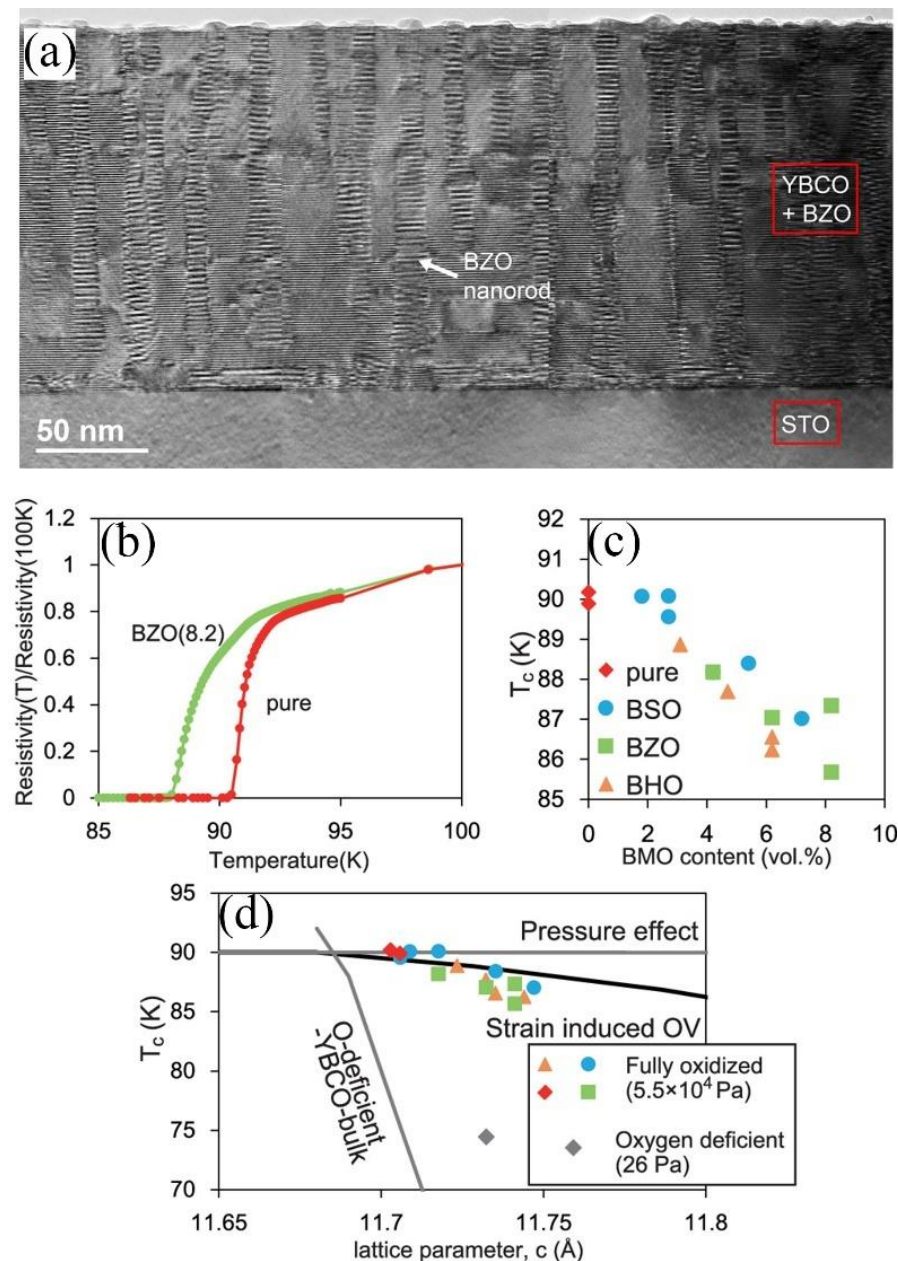

Figure 11. (**a**) BF-STEM image of the YBCO+BZO film. (**b**) T vs. normalized R in the pure YBCO and YBCO+BZO films. (**c**) T_c vs. B*M*O content in nanocomposite films. (**d**) T_c vs. *c*-lattice parameters. Reprinted with permission from Ref. [95]. Copyright 2017, American Chemical Society.

Cantoni et al. [90] showed that the oxygen composition of self-assembled superconducting films containing $BaZrO_3$ nanocolumns was strongly affected by nanoscale strain modulation. By increasing the concentration of $BaZrO_3$ nanocolumns, the *RE*BCO underwent a greater overall tensile strain along *c*-axis, leading to an increase in *c*-lattice parameter. Their finding explained the observed reduction in T_c. Nanostrain and corresponding effects

on anion composition had been demonstrated directly. Within a few nanometers of $BaZrO_3$ nanocolumns, the strain was localized.

4.6. Use of Buffer Layers to Release Strain

By modulating the lattice strain at the heterointerface of *REB*CO films, Akihito Mizuno et al. [97] aimed to realize superconducting diodes with rectifying properties. They fabricated $YBCO/PrBa_2Cu_3O_y$ (PrBCO) films to improve rectifying properties, where PrBCO was used to reduce the strain resulting from the lattice mismatch between YBCO films and CeO_2 substrates. Moreover, they assessed the rectification characteristics at different magnetic fields and temperatures to determine optimal operating conditions. Accordingly, they confirmed that maximum rectification was achieved at 0.096 T and 70 K, as shown in Figure 12.
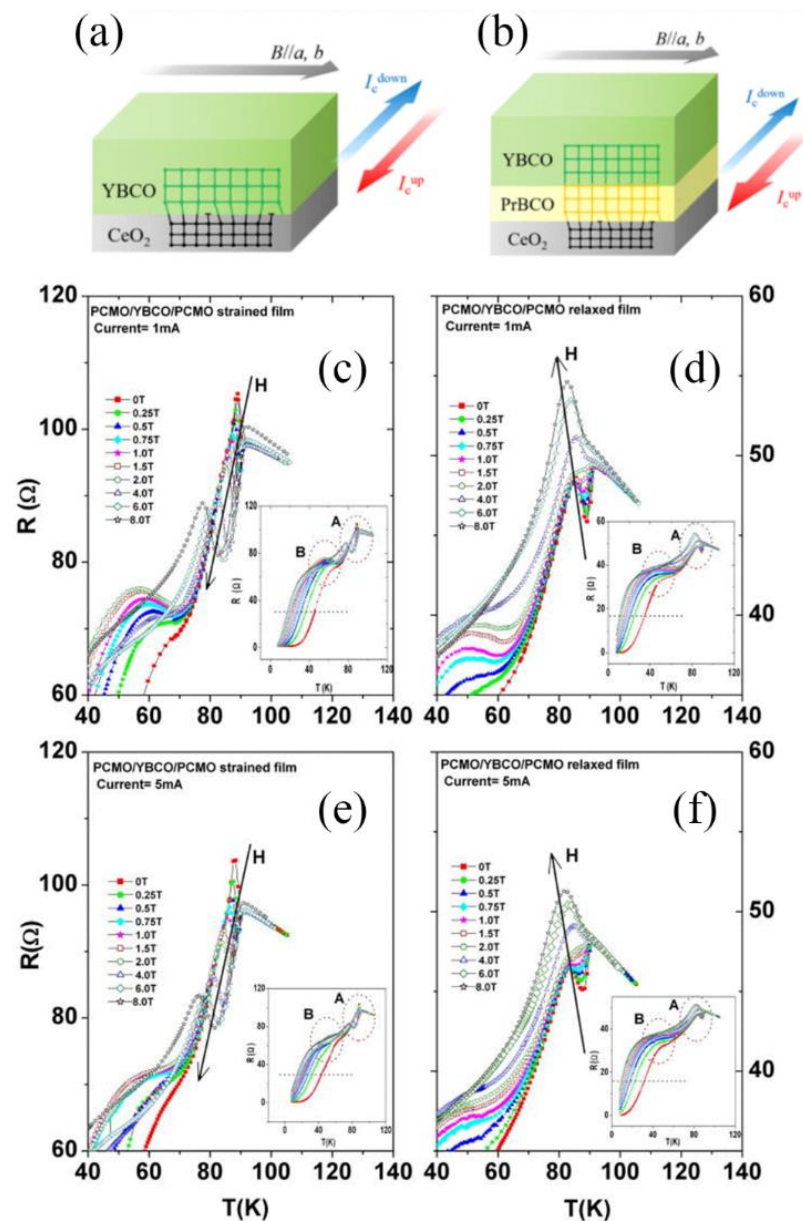

Figure 12. Schematic diagram of (**a**) YBCO and (**b**) YBCO/PrBCO films. Reprinted with permission from Ref. [97]. Copyright 2022, IEEE-Inst Electrical Electronics Engineers Inc. *T-R* behavior near the hump region at different applied *H* (0–8 T) for strained films (**c**) and relaxed films (**d**) at 1 mA applied current. (**e**) Strained film and (**f**) relaxed film at 5 mA applied current. Reprinted with permission from Ref. [98]. Copyright 2013, AIP Publishing.

Dipak Kumar Baisnab et al. [98] deposited trilayer films of $Pr_{0.5}Ca_{0.5}MnO_3$/YBCO/$Pr_{0.5}Ca_{0.5}MnO_3$ on MgO substrates by PLD. In one trilayer, the bottom $Pr_{0.5}Ca_{0.5}MnO_3$ layer was thin, and thus, subjected to strain induced by strain. However, in another trilayer, the bottom layer was thick enough to prevent such strain from occurring. To explore how charge-order melting and the formation of ferromagnetic clusters in $Pr_{0.5}Ca_{0.5}MnO_3$ films influence the superconductivity of YBCO, current and magnetic field-dependent resistance measurements were carried out on the trilayers at liquid helium temperatures. Compared with other trilayers, the suppression of strain on T_c of YBCO was relatively high. Based on the above data, the activation energy of vortex hopping in the sandwiched YBCO film was evaluated. The strained trilayer showed higher vortex pinning forces. Using strain, current and magnetic field simultaneously was found to be possible for controlling the superconducting behavior of sandwiched YBCO layers.

By DC magnetron sputtering, Yilun He et al. [99] grew epitaxial electron-doped infinite-layer $Sr_{0.9}La_{0.1}CuO_2$ (SLCO) films. As well as this, they investigated corresponding structural and electrical properties by varying the film thickness and reduction annealing time. The epitaxial buffer layers of $Ba_ySr_{1-y}TiO_3$ with y = 0.4, 0.55, and 0.7, deposited on (001) $(La_{0.18}Sr_{0.82})(Al_{0.59}Ta_{0.41})O_3$ (LSAT) substrates, were applied to introduce different types of strain to SLCO films. Short time reduction annealing of tensile strained SLCO films on $Ba_{0.55}Sr_{0.45}TiO_3$ and $Ba_{0.7}Sr_{0.3}TiO_3$ layers was proved to be effective for promoting superconductivity. However, reduction annealing was not effective for compressive strained SLCO films on $Ba_{0.4}Sr_{0.6}TiO_3$ layers. Additionally, superconducting properties of tensile strained SLCO films on $Ba_{0.55}Sr_{0.45}TiO_3$ and $Ba_{0.7}S_{r0.3}TiO_3$ layers were strongly dependent on thickness.

C. Park and D. P. Norton et al. [100] deposited superconducting YBCO/CeO_2/YSZ/CeO_2 multilayer on rolled-textured (001)Ni by PLD. YBCO films with relatively thick thickness achieved J_c greater than 1 MA/cm^2. Furthermore, I_c of YBCO films grown on rolling-assisted biaxially textured substrates was measured for their tensile and compressive bend strain tolerances. When applied compressive bend diameters up to 1.5 cm and tensile bend diameters up to 3.2 cm, these conductors retained up to 80% of their unstrained I_c. J_c degraded as a result of transverse cracks forming and propagating. These results suggested an association between oxide layer thickness and bend-strain tolerance.

5. Conclusions and Future Outlook

The impact of strain on superconductivity is significant. The interactions between the superconductivity with deformations of the crystal lattice have already been fulfilled in experiments. Condensed matter research has been driven by the desire to increase T_c by structural and chemical manipulation for many years.

At present, the corresponding theoretical research work has also made some progress. In general, HTSs are electronically inhomogeneous at the nanoscale. It is astonishing to find that cuprate superconductors exhibit a wide range of nanoscale inhomogeneities in vital properties, such as collective mode energy (Ω) [101], the spectral gap (Δ) [102,103], and even the pairing temperature (T_p) [104]. It has been debated for more than two decades which local variable is responsible for this electronic inhomogeneity. Among them, both strain [105] and dopants [106] have been empirically linked to electronic structure. Charge [107] or strain [108], or a carefully tuned combination of both [109], has been argued to be the dominant factor in theoretical models. The apical oxygen height has been closely linked to the superconducting pairing strength. Different strain theories predicted increased [17,18,110] or reduced [19] pairing strength with increasing apical oxygen height. Nevertheless, microscopic theories of reason and influence have been stalled by uncertainty about the location of dopants.

The large-scale application of superconductors in the fields of energy, information, transportation, space exploration, etc., will generate huge economic benefits. At the current stage, the application of superconductivity has not only stayed in the conceptual stage, but has been fully proven of feasibility. The emergence of new driving forces, such as

performance, cost-effectiveness, reliability, practicality and competitiveness of existing technologies are the research priorities for future large-scale superconducting practical application technologies.

In this review, we summarize the current progress of strain studies on cuprate superconductors. In summary, current strain studies on superconductors are still focused on the post-preparation performance testing and analysis stages. At the preparation stage, strain magnitude cannot be controlled systematically. Although some papers have mentioned that the parameters and film thickness at the preparation stage determine the strain magnitude of films, there is still a lack of systematic guidelines and methods on how to precisely regulate the strain magnitude of the film. In addition, since the current theoretical research on cuprate superconductors lags behind experimental research, the mechanism of the effect of strain on properties is still controversial, which also limits the further development of research on HTS materials. Strain is a factor that can significantly affect superconducting properties. How to achieve the low-cost, high-reliability application of stable and controllable strain is the next urgent goal. This needs to be explored in depth before the large-scale application of HTS films.

References

1. Wu, M.K.; Ashburn, J.R.; Torng, C.J.; Hor, P.H.; Meng, R.L.; Gao, L.; Huang, Z.J.; Wang, Y.Q.; Chu, C.W. Superconductivity at 93 K in a new mixed-phase Y-Ba-Cu-O compound system at ambient pressure. *Phys. Rev. Lett.* **1987**, *58*, 908–910. [CrossRef] [PubMed]
2. Schilling, A.; Cantoni, M.; Guo, J.D.; Ott, H.R. Superconductivity above 130 K in the Hg-Ba-Ca-Cu-O system. *Nature* **1993**, *363*, 56–58. [CrossRef]
3. Parkin, S.S.P.; Lee, V.Y.; Engler, E.M.; Nazzal, A.I.; Huang, T.C.; Gorman, G.; Savoy, R.; Beyers, R. Bulk superconductivity at 125 K in $Tl_2Ca_2Ba_2Cu_3O_x$. *Phys. Rev. Lett.* **1988**, *60*, 2539–2542. [CrossRef] [PubMed]
4. Maeda, H.; Tanaka, Y.; Fukutomi, M.; Asano, T. A New High-T_c Oxide Superconductor without a Rare Earth Element. *Jpn. J. Appl. Phys.* **1988**, *27*, L209–L210. [CrossRef]
5. Klein, N. High-frequency applications of high-temperature superconductor thin films. *Rep. Prog. Phys.* **2002**, *65*, 1387–1425. [CrossRef]
6. Simsek, Y.; Vlasko-Vlasov, V.; Koshelev, A.E.; Benseman, T.; Hao, Y.; Kesgin, I.; Claus, H.; Pearson, J.; Kwok, W.K.; Welp, U. Thick $Bi_2Sr_2CaCu_2O_{8+\delta}$ films grown by liquid-phase epitaxy for Josephson THz applications. *Supercond. Sci. Technol.* **2018**, *31*, 015009. [CrossRef]
7. Koch, R.H.; Umbach, C.P.; Clark, G.J.; Chaudhari, P.; Laibowitz, R.B. Quantum interference devices made from superconducting oxide thin films. *Appl. Phys. Lett.* **1987**, *51*, 200–202. [CrossRef]
8. Zeljkovic, I.; Nieminen, J.; Huang, D.; Chang, T.R.; He, Y.; Jeng, H.T.; Xu, Z.; Wen, J.; Gu, G.; Lin, H.; et al. Nanoscale interplay of strain and doping in a high-temperature superconductor. *Nano Lett.* **2014**, *14*, 6749–6753. [CrossRef]
9. Foltyn, S.R.; Wang, H.; Civale, L.; Maiorov, B.; Jia, Q.X. The role of interfacial defects in enhancing the critical current density of $YBa_2Cu_3O_{7-\delta}$ coatings. *Supercond. Sci. Technol.* **2009**, *22*, 125002–125005. [CrossRef]
10. Locquet, J.-P.; Perret, J.; Fompeyrine, J.; Mächler, E.; Seo, J.W.; Tendeloo, G.V. Doubling the critical temperature of $La_{1.9}Sr_{0.1}CuO_4$ using epitaxial strain. *Nature* **1998**, *194*, 453–456. [CrossRef]
11. Bagués, N.; Santiso, J.; Esser, B.D.; Williams, R.E.A.; McComb, D.W.; Konstantinovic, Z.; Balcells, L.; Sandiumenge, F. The misfit dislocation core phase in complex oxide heteroepitaxy. *Adv. Funct. Mater.* **2018**, *28*, 1704437. [CrossRef]
12. Arredondo, M.; Ramasse, Q.M.; Weyland, M.; Mahjoub, R.; Vrejoiu, I.; Hesse, D.; Browning, N.D.; Alexe, M.; Munroe, P.; Nagarajan, V. Direct Evidence for Cation Non-Stoichiometry and Cottrell Atmospheres Around Dislocation Cores in Functional Oxide Interfaces. *Adv. Mater.* **2010**, *22*, 2430–2434. [CrossRef] [PubMed]
13. Sugano, M.; Shikimachi, K.; Hirano, N.; Nagaya, S. The reversible strain effect on critical current over a wide range of temperatures and magnetic fields for YBCO coated conductors. *Supercond. Sci. Technol.* **2010**, *23*, 085013. [CrossRef]
14. Sugano, M.; Nakamura, T.; Manabe, T.; Shikimachi, K.; Hirano, N.; Nagaya, S. The intrinsic strain effect on critical current under a magnetic field parallel to the *c* axis for a MOCVD-YBCO-coated conductor. *Supercond. Sci. Technol.* **2008**, *21*, 115019. [CrossRef]

15. Cheggour, N.; Ekin, J.W.; Clickner, C.C.; Verebelyi, D.T.; Thieme, C.L.H.; Feenstra, R.; Goyal, A. Reversible axial-strain effect and extended strain limits in Y-Ba-Cu-O coatings on deformation-textured substrates. *Appl. Phys. Lett.* **2003**, *83*, 4223–4225. [CrossRef]

16. Pavarini, E.; Dasgupta, I.; Saha-Dasgupta, T.; Jepsen, O.; KAndersen, O. Band-structure trend in hole-doped cuprates and correlation with $T_{c\,max}$. *Phys. Rev. Lett.* **2001**, *87*, 047003. [CrossRef]

17. Bergman, D.L.; Pereg-Barnea, T. The origin of T_c enhancement in heterostructure cuprate superconductors. *Materials* **2011**, *4*, 1835–1845. [CrossRef]

18. Ohta, Y.; Tohyama, T.; Maekawa, S. Apex oxygen and critical temperature in copper oxide superconductors: Universal correlation with the stability of local singlets. *Phys. Rev. B Condens. Matter* **1991**, *43*, 2968–2982. [CrossRef]

19. Mori, M.; Khaliullin, G.; Tohyama, T.; Maekawa, S. Origin of spatial variation of pairing gap in Bi-based high-T_c cuprates. *Phys. Rev. Lett.* **2008**, *101*, 3382–3390. [CrossRef]

20. Locquet, J.-P.; Williams, L.J. Epitaxially induced defects in Sr- and O-doped La_2CuO_4 thin films grown by MBE: Implications for transport properties. *Acta Phys. Pol. A* **1997**, *92*, 69–84. [CrossRef]

21. van der Laan, D.C.; Ekin, J.W.; Douglas, J.F.; Clickner, C.C.; Stauffer, T.C.; Goodrich, L.F. Effect of strain, magnetic field and field angle on the critical current density of $YBa_2Cu_3O_{7-\delta}$ coated conductors. *Supercond. Sci. Technol.* **2010**, *23*, 072001. [CrossRef]

22. Sato, H.; Hiramatsu, H.; Kamiya, T.; Hosono, H. Strain Engineering at Heterointerfaces: Application to an Iron Pnictide Superconductor, Cobalt-Doped $BaFe_2As_2$. *ACS Appl. Mater. Inter.* **2020**, *12*, 50096–50104. [CrossRef] [PubMed]

23. Yu, J.; Li, F.; Fan, J.; Muhammad, S.; Dahal, Y.P.; Zhang, Z.; Wang, S. Macroscopic residual stress and properties in different $YBa_2Cu_3O_{7-x}$ heterogeneous systems. *Phys. C Supercond. Its Appl.* **2020**, *577*, 1353728. [CrossRef]

24. Li, Z.; Coll, M.; Mundet, B.; Palau, A.; Puig, T.; Obradors, X. Suppression of superconductivity at the nanoscale in chemical solution derived $YBa_2Cu_3O_{7-\delta}$ thin films with defective $Y_2Ba_4Cu_8O_{16}$ intergrowths. *Nanoscale Adv.* **2020**, *2*, 3384–3393. [CrossRef]

25. Osamura, K.; Machiya, S.; Tsuchiya, Y.; Suzuki, H. Force free strain exerted on a YBCO layer at 77 K in surround Cu stabilized YBCO coated conductors. *Supercond. Sci. Technol.* **2010**, *23*, 045020. [CrossRef]

26. Favre, S.; Ariosa, D.; Yelpo, C.; Mazini, M.; Faccio, R. Depression of critical temperature due to residual strain induced by PLD deposition on $YBa_2Cu_3O_{7-\delta}$ thin films. *Mater. Chem. Phys.* **2021**, *266*, 124507. [CrossRef]

27. Koblischka-Veneva, A.; Koblischka, M.R. Residual Stress/Strain Analysis of Bulk YBCO Superconductors Using EBSD. *IEEE Trans. Appl. Supercond.* **2022**, *32*, 1–5. [CrossRef]

28. Zhang, J.; Wang, W.; Wang, T.; Jiang, L.; Wang, N.; Dai, Y.; Wang, M.; Qi, Y. Atomic-scale analysis of the interface structure and lattice mismatch relaxation of $Bi_2Sr_2CaCu_2O_{8+\delta}/SrTiO_3$ heterostructure. *Ceram. Int.* **2021**, *47*, 8722–8727. [CrossRef]

29. Zhang, J.; Wang, W.; Wang, N.; Wang, M.; Qi, Y. Atomic-resolution study on the interface structure and strain state reversion of the $Bi_2Sr_2CuO_{6+\delta}/MgO$ heterostructure. *J. Colloid Interf. Sci.* **2021**, *592*, 291–295. [CrossRef]

30. Wang, Y.; Liu, X.P.; Qin, G.W. Strain analysis of misfit dislocations in α-Fe_2O_3/α-Al_2O_3 heterostructure interface by geometric phase analysis. *Micron* **2015**, *69*, 21–24. [CrossRef]

31. Hÿtch, M.J.; Snoeck, E.; Kilaas, R. Quantitative measurement of displacement and strain fields from HREM micrographs. *Ultramicroscopy* **1998**, *74*, 131–146. [CrossRef]

32. Bierwolf, R.; Hohenstein, M.; Phillipp, F.; Brandt, O.; Crook, G.E.; Ploog, K. Direct measurement of local lattice distortions in strained layer structures by HREM. *Ultramicroscopy* **1993**, *49*, 273–285. [CrossRef]

33. Zhu, Y.; Ophus, C.; Ciston, J.; Wang, H. Interface lattice displacement measurement to 1 pm by geometric phase analysis on aberration-corrected HAADF STEM images. *Acta Materialia* **2013**, *61*, 5646–5663. [CrossRef]

34. Uesugi, F.; Hokazono, A.; Takeno, S. Evaluation of two-dimensional strain distribution by STEM/NBD. *Ultramicroscopy* **2011**, *111*, 995–998. [CrossRef] [PubMed]

35. Usuda, K.; Numata, T.; Irisawa, T.; Hirashita, N.; Takagi, S. Strain characterization in SOI and strained-Si on SGOI MOSFET channel using nano-beam electron diffraction (NBD). *Mater. Sci. Eng. B* **2005**, *124–125*, 143–147. [CrossRef]

36. Armigliato, A.; Balboni, R.; Carnevale, G.P.; Pavia, G.; Piccolo, D.; Frabboni, S.; Benedetti, A.; Cullis, A.G. Application of convergent beam electron diffraction to two-dimensional strain mapping in silicon devices. *Appl. Phys. Lett.* **2003**, *82*, 2172–2174. [CrossRef]

37. Hÿtch, M.; Houdellier, F.; Hüe, F.; Snoeck, E. Nanoscale holographic interferometry for strain measurements in electronic devices. *Nature* **2008**, *453*, 1086–1089. [CrossRef] [PubMed]

38. Hÿtch, M.J.; Minor, A.M. Observing and measuring strain in nanostructures and devices with transmission electron microscopy. *MRS Bull.* **2014**, *39*, 138–146. [CrossRef]

39. Cooper, D.; Denneulin, T.; Bernier, N.; Beche, A.; Rouviere, J.L. Strain mapping of semiconductor specimens with nm-scale resolution in a transmission electron microscope. *Micron* **2016**, *80*, 145–165. [CrossRef]

40. Beche, A.; Rouviere, J.L.; Barnes, J.P.; Cooper, D. Strain measurement at the nanoscale: Comparison between convergent beam electron diffraction, nano-beam electron diffraction, high resolution imaging and dark field electron holography. *Ultramicroscopy* **2013**, *131*, 10–23. [CrossRef]

41. Okada, H.; Takahashi, H.; Matsuishi, S.; Hirano, M.; Hosono, H.; Matsubayashi, K.; Uwatoko, Y.; Takahashi, H. Pressure dependence of the superconductor transition temperature of $Ca(Fe_{1-x}Cox)AsF$ compounds: A comparison with the effect of pressure on $LaFeAsO_{1-x}F_x$. *Phys. Rev. B* **2010**, *81*, 054507. [CrossRef]

42. Chen, X.J.; Struzhkin, V.V.; Yu, Y.; Goncharov, A.F.; Lin, C.T.; Mao, H.K.; Hemley, R.J. Enhancement of superconductivity by pressure-driven competition in electronic order. *Nature* **2010**, *466*, 950–953. [CrossRef] [PubMed]

43. Takahashi, H.; Igawa, K.; Arii, K.; Kamihara, Y.; Hirano, M.; Hosono, H. Superconductivity at 43 K in an iron-based layered compound LaO$_{1-x}$F$_x$FeAs. *Nature* **2008**, *453*, 376–378. [CrossRef] [PubMed]

44. Si, W.; Li, H.-C.; Xi, X. Strain and oxygenation effects on superconductivity of La$_{1.85}$Sr$_{0.15}$CuO$_4$ thin films. *Appl. Phys. Lett.* **1999**, *74*, 2839–2841. [CrossRef]

45. Nakamura, F.; Goko, T.; Hori, J.; Uno, Y.; Kikugawa, N.; Fujita, T. Role of two-dimensional electronic state in superconductivity in La$_{2-x}$Sr$_x$CuO$_4$. *Phys. Rev. B* **2000**, *61*, 107–110. [CrossRef]

46. Si, W.; Xi, X. Epitaxial-strain-induced insulator-superconductor transition in undoped and lightly doped La$_2$CuO$_4$. *Appl. Phys. Lett.* **2001**, *78*, 240–242. [CrossRef]

47. Zeng, X.; Si, W.; Stum, Z.; Xi, X. Doping dependence of superconducting properties in pulsed-laser-deposited La$_{2-x}$Sr$_x$CuO$_{4+\delta}$ thin films. *IEEE Trans. Appl. Supercond.* **2001**, *11*, 3213–3216. [CrossRef]

48. Bozovic, I.; Logvenov, G.; Belca, I.; Narimbetov, B.; Sveklo, I. Epitaxial strain and superconductivity in La$_{2-x}$Sr$_x$CuO$_4$ thin films. *Phys. Rev. Lett.* **2002**, *89*, 107001. [CrossRef]

49. Choi, E.M.; Zhu, B.; Lu, P.; Feighan, J.; Sun, X.; Wang, H.; MacManus-Driscoll, J.L. Magnetic signatures of 120 K superconductivity at interfaces in La$_2$CuO$_{4+\delta}$. *Nanoscale* **2020**, *12*, 3157–3165. [CrossRef]

50. Sato, H.; Tsukada, A.; Naito, M.; Matsuda, A. La$_{2-x}$Sr$_x$CuO$_y$ epitaxial thin films (x = 0 to 2): Structure, strain, and superconductivity. *Phys. Rev. B* **2000**, *61*, 12447–12456. [CrossRef]

51. Zaytseva, I.; Minikayev, R.; Dobročka, E.; Španková, M.; Bruyant, N.; Cieplak, M.Z. Structural properties and magnetoresistance of La$_{1.952}$Sr$_{0.048}$CuO$_4$ thin films. *J. Appl. Phys.* **2020**, *127*, 073901. [CrossRef]

52. Wang, Y.; Wang, R.-F.; Zhang, Q.; Liao, M.; Gu, L.; Zhang, D.; Song, C.-L.; Ma, X.-C.; Xue, Q.-K. Co-deposition growth and superconductivity of La$_{2-x}$Sr$_x$CuO$_4$ films by reactive molecular beam epitaxy. *Phys. Rev. B* **2021**, *103*, 184514. [CrossRef]

53. Zhang, X.; Zhao, H.; Zhu, J. Visualization and control of oxygen dopant ordering in a cuprate superconductor. *Mater. Today Phys.* **2022**, *23*, 100629. [CrossRef]

54. Petricek, V.; Gao, Y.; Lee, P.; Coppens, P. X-ray analysis of the incommensurate modulation in the 2:2:1:2 Bi-Sr-Ca-Cu-O superconductor including the oxygen atoms. *Phys. Rev. B* **1990**, *42*, 387–392. [CrossRef]

55. Le, P.Y.; Mckinnon, W.R.; Tarascon, J.; Barboux, P. Origin of the incommensurate modulation of the 80-K superconductor Bi$_2$Sr$_2$CaCu$_2$O$_{8.21}$ derived from isostructural commensurate Bi$_{10}$Sr$_{15}$Fe$_{10}$O$_{46}$. *Phys. Rev. B* **1989**, *40*, 6810–6816. [CrossRef]

56. Subramanian, M.A.; Torardi, C.C.; Calabrese, J.C.; Gopalakrishnan, J.; Morrissey, K.J.; Askew, T.R.; Flippen, R.B.; Chowdhry, U.; Sleight, A.W. A New High-Temperature Superconductor: Bi$_2$Sr$_{3-x}$Ca$_x$Cu$_2$O$_{8+y}$. *Science* **1988**, *239*, 1015–1017. [CrossRef]

57. Zeljkovic, I.; Main, E.J.; Williams, T.L.; Boyer, M.C.; Chatterjee, K.; Wise, W.D.; Yin, Y.; Zech, M.; Pivonka, A.; Kondo, T.; et al. Scanning tunnelling microscopy imaging of symmetry-breaking structural distortion in the bismuth-based cuprate superconductors. *Nat. Mater.* **2012**, *11*, 585–589. [CrossRef]

58. Haken, B.t.; Kate, H.H.J.t.; Tenbrink, J. Compressive and tensile axial strain reduced critical currents in Bi-2212 conductors. *IEEE Trans. Appl. Supercond.* **1995**, *5*, 1298–1301. [CrossRef]

59. Sunwong, P.; Higgins, J.S.; Hampshire, D.P. Angular, Temperature, and Strain Dependencies of the Critical Current of DI-BSCCO Tapes in High Magnetic Fields. *IEEE Trans. Appl. Supercond.* **2011**, *21*, 2840–2844. [CrossRef]

60. Forro, L.; Ilakovac, V.V.; Keszei, B. High-pressure study of Bi$_2$Sr$_2$CaCu$_2$O$_8$ single crystals. *Phys. Rev. B Condens. Matter.* **1990**, *41*, 9551–9554. [CrossRef]

61. Klotz, S.; Schilling, J.S. Hydrostatic pressure dependence of the superconducting transition temperature to 7 GPa in Bi$_2$Ca$_1$Sr$_2$Cu$_2$O$_{8+y}$ as a function of oxygen content. *Phys. C Supercond.* **1993**, *209*, 499–506. [CrossRef]

62. Chen, X.-J.; Struzhkin, V.V.; Hemley, R.J.; Mao, H.-K.; Kendziora, C. High-pressure phase diagram of Bi$_2$Sr$_2$CaCu$_2$O$_{8+\delta}$ single crystals. *Phys. Rev. B* **2004**, *70*, 214502. [CrossRef]

63. Song, D.; Zhang, X.; Lian, C.; Liu, H.; Alexandrou, I.; LaziĆ, I.; G, E.; Bosch, T.; Zhang, D.; Wang, L.; et al. Visualization of Dopant Oxygen Atoms in a Bi$_2$Sr$_2$CaCu$_2$O$_{8+\delta}$ Superconductor. *Adv. Funct. Mater.* **2019**, 1603843–1603848. [CrossRef]

64. Mundet, B.; Hartman, S.T.; Guzman, R.; Idrobo, J.C.; Obradors, X.; Puig, T.; Mishra, R.; Gazquez, J. Local strain-driven migration of oxygen vacancies to apical sites in YBa$_2$Cu$_3$O$_{7-x}$. *Nanoscale* **2020**, *12*, 5922–5931. [CrossRef]

65. Laan, D.C.v.d.; Ekin, J.W. Large intrinsic effect of axial strain on the critical current of high-temperature superconductors for electric power applications. *Appl. Phys. Lett.* **2007**, *90*, 052506. [CrossRef]

66. Barth, C.; Weiss, K.P.; Goldacker, W. Influence of shear stress on current carrying capabilities of high temperature superconductor tapes. *IEEE Trans. Appl. Supercond.* **2011**, *21*, 3098–3101. [CrossRef]

67. van der Laan, D.C.; Haugan, T.J.; Barnes, P.N. Effect of a compressive uniaxial strain on the critical current density of grain boundaries in superconducting YBa$_2$Cu$_3$O$_{7-\delta}$ films. *Phys. Rev. Lett.* **2009**, *103*, 027005. [CrossRef]

68. Guzman, R.; Gazquez, J.; Mundet, B.; Coll, M.; Obradors, X.; Puig, T. Probing localized strain in solution-derived YBa$_2$Cu$_3$O$_{7-\delta}$ nanocomposite thin films. *Phys. Rev. Mater.* **2017**, *1*, 024801. [CrossRef]

69. Yugay, K.N.; Muravjev, A.V.; Seropyan, G.M.; Konovalenko, K.B.; Huh, Y. Thin films of high-T_c YBCO with frozen strains. *Low Temp. Phys.* **2006**, *32*, 55–60. [CrossRef]

70. Obradors, X.; Martínez-Julián, F.; Zalamova, K.; Vlad, V.R.; Pomar, A.; Palau, A.; Llordés, A.; Chen, H.; Coll, M.; Ricart, S.; et al. Nucleation and mesostrain influence on percolating critical currents of solution derived YBa$_2$Cu$_3$O$_7$ superconducting thin films. *Phys. C Supercond. Its Appl.* **2012**, *482*, 58–67. [CrossRef]

71. Pahlke, P.; Trommler, S.; Holzapfel, B.; Schultz, L.; Hühne, R. Dynamic variation of biaxial strain in optimally doped and underdoped YBa$_2$Cu$_3$O$_{7-\delta}$ thin films. *J. Appl. Phys.* **2013**, *113*, 123907. [CrossRef]

72. Putzky, D.; Radhakrishnan, P.; Wang, Y.; Wochner, P.; Christiani, G.; Minola, M.; van Aken, P.A.; Logvenov, G.; Benckiser, E.; Keimer, B. Strain-induced structural transition in DyBa$_2$Cu$_3$O$_{7-x}$ films grown by atomic layer-by-layer molecular beam epitaxy. *Appl. Phys. Lett.* **2020**, *117*, 072601. [CrossRef]

73. Tan, S.; Zhang, Y.; Xia, M.; Ye, Z.; Chen, F.; Xie, X.; Peng, R.; Xu, D.; Fan, Q.; Xu, H. Interface-induced superconductivity and strain-dependent spin density waves in FeSe/SrTiO$_3$ thin films. *Nat. Mater.* **2013**, *12*, 634–640. [CrossRef] [PubMed]

74. He, S.; He, J.; Zhang, W.; Zhao, L.; Liu, D.; Liu, X.; Mou, D.; Ou, Y.-B.; Wang, Q.-Y.; Li, Z. Phase diagram and electronic indication of high-temperature superconductivity at 65 K in single-layer FeSe films. *Nat. Mater.* **2013**, *12*, 605–610. [CrossRef]

75. Ge, J.-F.; Liu, Z.-L.; Liu, C.; Gao, C.-L.; Qian, D.; Xue, Q.-K.; Liu, Y.; Jia, J.-F. Superconductivity above 100 K in single-layer FeSe films on doped SrTiO$_3$. *Nat. Mater.* **2015**, *14*, 285–289. [CrossRef]

76. Zhang, S.J.; Wang, X.C.; Sammynaiken, R.; Tse, J.S.; Yang, L.X.; Li, Z.; Liu, Q.Q.; Desgreniers, S.; Yao, Y.; Liu, H.Z.; et al. Effect of pressure on the iron arsenide superconductor Li$_x$FeAs (x = 0.8, 1.0, 1.1). *Phys. Rev. B* **2009**, *80*, 014056. [CrossRef]

77. Ekin, J.W. Effect of transverse compressive stress on the critical current and upper critical field of Nb$_3$Sn. *J. Appl. Phys.* **1987**, *62*, 4829–4834. [CrossRef]

78. Ekin, J.W. Strain scaling law for flux pinning in practical superconductors. Part 1: Basic relationship and application to Nb$_3$Sn conductors. *Cryogenics* **1980**, *20*, 611–624. [CrossRef]

79. Keys, S.A.; Koizumi, N.; Hampshire, D.P. The strain and temperature scaling law for the critical current density of a jelly-roll Nb$_3$Al strand in high magnetic fields. *Supercond. Sci. Technol.* **2002**, *15*, 991–1010. [CrossRef]

80. Markiewicz, W.D. Comparison of strain scaling functions for the strain dependence of composite Nb$_3$Sn superconductors. *Supercond. Sci. Technol.* **2008**, *21*, 054004. [CrossRef]

81. Lu, X.F.; Taylor, D.M.J.; Hampshire, D.P. Critical current scaling laws for advanced Nb$_3$Sn superconducting strands for fusion applications with six free parameters. *Supercond. Sci. Technol.* **2008**, *21*, 105016. [CrossRef]

82. Pogrebnyakov, A.V.; Redwing, J.M.; Raghavan, S.; Vaithyanathan, V.; Schlom, D.G.; Xu, S.Y.; Li, Q.; Tenne, D.A.; Soukiassian, A.; Xi, X.X.; et al. Enhancement of the Superconducting Transition Temperature of MgB$_2$ by a Strain-Induced Bond-Stretching Mode Softening. *Phys. Rev. Lett.* **2004**, *93*, 147006. [CrossRef] [PubMed]

83. Liu, Y.-C.; Wang, W.-S.; Zhang, F.-C.; Wang, Q.-H. Superconductivity in Sr$_2$RuO$_4$ thin films under biaxial strain. *Phys. Rev. B* **2018**, *97*, 224522. [CrossRef]

84. Ahadi, K.; Galletti, L.; Li, Y.; Salmani-Rezaie, S.; Wu, W.; Stemmer, S. Enhancing superconductivity in SrTiO$_3$ films with strain. *Sci. Adv.* **2019**, *5*, eaaw0120. [CrossRef] [PubMed]

85. Mano, P.; Minamitani, E.; Watanabe, S. Straintronic effect for superconductivity enhancement in Li-intercalated bilayer MoS$_2$. *Nanoscale Adv.* **2020**, *2*, 3150–3155. [CrossRef]

86. Llordés, A.; Palau, A.; Gázquez, J.; Coll, M.; Vlad, R.; Pomar, A.; Arbiol, J.; Guzmán, R.; Ye, S.; Rouco, V.; et al. Nanoscale strain-induced pair suppression as a vortex-pinning mechanism in high-temperature superconductors. *Nat. Mater.* **2012**, *11*, 329–336. [CrossRef]

87. Li, Z.; Coll, M.; Mundet, B.; Chamorro, N.; Valles, F.; Palau, A.; Gazquez, J.; Ricart, S.; Puig, T.; Obradors, X. Control of nanostructure and pinning properties in solution deposited YBa$_2$Cu$_3$O$_{7-x}$ nanocomposites with preformed perovskite nanoparticles. *Sci. Rep.* **2019**, *9*, 5828. [CrossRef]

88. Cayado, P.; Mundet, B.; Eloussifi, H.; Vallés, F.; Coll, M.; Ricart, S.; Gázquez, J.; Palau, A.; Roura, P.; Farjas, J.; et al. Epitaxial superconducting GdBa$_2$Cu$_3$O$_{7-\delta}$/Gd$_2$O$_3$ nanocomposite thin films from advanced low-fluorine solutions. *Supercond. Sci. Technol.* **2017**, *30*, 125010. [CrossRef]

89. Solano, E.; Geenen, F.; Puig, T.; Obradors, X.; Mocuta, C.; Detavernier, C. Axiotaxy in oxide heterostructures: Preferential orientation of BaCeO$_3$ nanoparticles embedded in superconducting YBa$_2$Cu$_3$O$_{7-\delta}$ thin films. *Thin Solid Films* **2017**, *638*, 105–113. [CrossRef]

90. Cantoni, C.; Gao, Y.; Wee, S.H.; Specht, E.D.; Gazquez, J.; Meng, J.; Pennycook, S.J.; Goyal, A. Strain-driven oxygen deficiency in self-assembled, nanostructured, composite oxide films. *ACS Nano* **2011**, *5*, 4783–4789. [CrossRef]

91. Ye, J.; Mou, S.; Zhu, R.; Liu, L.; Li, Y. Effect and Mechanism of Doping Concentration on Growth and Performance of Thick BaHfO$_3$-doped Y$_{0.5}$Gd$_{0.5}$Ba$_2$Cu$_3$O$_{7-\delta}$ Films by Pulsed Laser Deposition. *J. Supercond. Nov. Magn.* **2022**, *35*, 435–444. [CrossRef]

92. Miura, S.; Yoshida, Y.; Ichino, Y.; Matsumoto, K.; Ichinose, A.; Awaji, S. Characteristics of high-performance BaHfO$_3$-doped SmBa$_2$Cu$_3$O$_y$ superconducting films fabricated with a seed layer and low-temperature growth. *Supercond. Sci. Technol.* **2015**, *28*, 065013. [CrossRef]

93. Ichino, Y.; Sato, S.; Tsuchiya, Y.; Yoshida, Y. Effect on SmBa$_2$Cu$_3$O$_y$ films of lattice strain induced by BaHfO$_3$ nanorods. *Phys. C Supercond. Its Appl.* **2020**, *575*, 1353692. [CrossRef]

94. Samoilenkov, S.V.; Boytsova, O.V.; Amelichev, V.A.; Kaul, A.R. Anisotropic strain of BaZrO$_3$, BaCeO$_3$ and Y$_2$O$_3$ nanoinclusions in a YBa$_2$Cu$_3$O$_{7-x}$ epitaxial film matrix and its relation to the oxygen content of the superconductor. *Supercond. Sci. Technol.* **2011**, *24*, 055003. [CrossRef]

95. Horide, T.; Kametani, F.; Yoshioka, S.; Kitamura, T.; Matsumoto, K. Structural evolution induced by interfacial lattice mismatch in self-organized YBa$_2$Cu$_3$O$_{7-\delta}$ nanocomposite film. *ACS Nano* **2017**, *11*, 1780–1788. [CrossRef]

96. Gondo, M.; Yoshida, M.; Yoshida, Y.; Ishimaru, M.; Horide, T.; Matsumoto, K.; Kita, R. Nanostructures and flux pinning properties in $YBa_2Cu_3O_{7-y}$ thin films with double perovskite Ba_2LuNbO_6 nanorods. *J. Appl. Phys.* **2021**, *129*, 195301. [CrossRef]

97. Mizuno, A.; Tsuchiya, Y.; Awaji, S.; Yoshida, Y. Rectification at various temperatures in $YBa_2Cu_3O_y$ coated conductors with $PrBa_2Cu_3O_y$ buffer layers. *IEEE Trans. Appl. Supercond.* **2022**, *32*, 1–5. [CrossRef]

98. Kumar Baisnab, D.; Janawadkar, M.P.; Sharma, S.; Sarguna, R.M.; Vaidhyanathan, L.S.; Bharathi, A. The effects of strain, current, and magnetic field on superconductivity in $Pr_{0.5}Ca_{0.5}MnO_3/YBa_2Cu_3O_7/Pr_{0.5}Ca_{0.5}MnO_3$ trilayer. *J. Appl. Phys.* **2013**, *113*, 113902. [CrossRef]

99. He, Y.; Ito, M.; Sakuma, K.; Ueda, K.; Asano, H. Preparation and Properties of $Sr_{0.9}La_{0.1}CuO_2$ Thin Films Grown on $BaySr_{1-y}TiO_3$ Layers. *IEEE Trans. Appl. Supercond.* **2015**, *25*, 1–4. [CrossRef]

100. Park, C.; Norton, D.P.; Budai, J.D.; Christen, D.K.; Verebelyi, D.; Feenstra, R.; Lee, D.F.; Goyal, A.; Kroeger, D.M.; Paranthaman, M. Bend strain tolerance of critical currents for $YBa_2Cu_3O_7$ films deposited on rolled-textured (001)Ni. *Appl. Phys. Lett.* **1998**, *73*, 1904–1906. [CrossRef]

101. Lee, J.; Fujita, K.; McElroy, K.; Slezak, J.A.; Wang, M.; Aiura, Y.; Bando, H.; Ishikado, M.; Masui, T.; Zhu, J.X.; et al. Interplay of electron–lattice interactions and superconductivity in $Bi_2Sr_2CaCu_2O_{8+\delta}$. *Nature* **2006**, *442*, 546–550. [CrossRef] [PubMed]

102. Pan, S.H.; O'Neal, J.P.; Badzey, R.L.; Chamon, C.; Ding, H.; Engelbrecht, J.R.; Wang, Z.; Eisaki, H.; Uchida, S.; Gupta, A.K.; et al. Microscopic electronic inhomogeneity in the high-T_c superconductor $Bi_2Sr_2CaCu_2O_{8+\delta}$. *Nature* **2001**, *413*, 282–285. [CrossRef] [PubMed]

103. Lang, K.M.; Madhavan, V.; Hoffman, J.E.; Hudson, E.W.; Eisaki, H.; Uchida, S.; Davis, J.C. Imaging the granular structure of high-T_c superconductivity in underdoped $Bi_2Sr_2CaCu_2O_{8+\delta}$. *Nature* **2002**, *415*, 412–416. [CrossRef] [PubMed]

104. Gomes, K.K.; Pasupathy, A.N.; Pushp, A.; Ono, S.; Ando, Y.; Yazdani, A. Visualizing pair formation on the atomic scale in the high-T_c superconductor $Bi_2Sr_2CaCu_2O_{8+\delta}$. *Nature* **2007**, *447*, 569–572. [CrossRef]

105. Slezak, J.A.; Lee, J.; Wang, M.; McElroy, K.; Fujita, K.; Andersen, B.M.; Hirschfeld, P.J.; Eisaki, H.; Uchida, S.; Davis, J.C. Imaging the impact on cuprate superconductivity of varying the interatomic distances within individual crystal unit cells. *Proc. Natl. Acad. Sci. USA* **2008**, *105*, 3203–3208. [CrossRef]

106. Zeljkovic, I.; Hoffman, J.E. Interplay of chemical disorder and electronic inhomogeneity in unconventional superconductors. *Phys. Chem. Chem. Phys. PCCP* **2013**, *15*, 13462–13478. [CrossRef]

107. Martin, I.; Balatsky, A.V. Doping-induced inhomogeneity in high-T_c superconductors. *Phys. C* **2001**, *357*, 46–48. [CrossRef]

108. Nunner, T.S.; Andersen, B.M.; Melikyan, A.; Hirschfeld, P.J. Dopant-modulated pair interaction in cuprate superconductors. *Phys. Rev. Lett.* **2005**, *95*, 177003. [CrossRef]

109. Chen, W.; Gabay, M.; Hirschfeld, P.J. Doping dependence of gap inhomogeneities at $Bi_2Sr_2CaCu_2O_{8+\delta}$ surfaces. *New J. Phys.* **2012**, *14*, 033004. [CrossRef]

110. Raimondi, R.; Jefferson, J.H.; Feiner, L.F. Effective single-band models for the high-T_c cuprates. II. Role of apical oxygen. *Phys. Rev. B* **1996**, *53*, 8774–8788. [CrossRef]